Markedly different impacts of primary emissions and secondary aerosol formation on aerosol mixing states revealed by simultaneous measurements of CCNC, V/HTDMA, and SP2

Jiangchuan Tao[1,8], Biao Luo[1,8], Weiqi Xu[3], Gang Zhao[6], Hanbin Xu[5], Biao Xue[1,8], Miaomiao Zhai[1,8], Wanyun Xu[4], Huarong Zhao[7], Sanxue Ren[7], Guangsheng Zhou[7], Li Liu[2,*], Ye Kuang[1,8,*] , Yele Sun[3]

[1] Institute for Environmental and Climate Research, Jinan University, Guangzhou, Guangdong, China

[2] Key Laboratory of Regional Numerical Weather Prediction, Institute of Tropical and Marine Meteorology, China Meteorological Administration, Guangzhou, China.

[3] State Key Laboratory of Atmospheric Boundary Layer Physics and Atmospheric Chemistry, Institute of Atmospheric Physics, Chinese Academy of Sciences, Beijing, China.

[4] State Key Laboratory of Severe Weather, Key Laboratory for Atmospheric Chemistry, Institute of Atmospheric Composition, Chinese Academy of Meteorological Sciences, Beijing, China

[5] Experimental Teaching Center, Sun Yat-Sen University, Guangzhou, China

[6] State Key Joint Laboratory of Environmental Simulation and Pollution Control, International Joint Laboratory for Regional Pollution Control, Ministry of Education, College of Environmental Sciences and Engineering, Peking University, Beijing 100871, China

[7] Hebei Gucheng Agricultural Meteorology National Observation and Research Station, Chinese Academy of Meteorological Sciences, Beijing, 100081, China

[8] Guangdong-Hongkong-Macau Joint Laboratory of Collaborative Innovation for Environmental Quality, Jinan University, Guangzhou, Guangdong, China

Correspondence: Ye Kuang (kuangye@jnu.edu.cn), Li Liu (liul@gd121.cn)

Abstract

The aerosol mixing state is a crucial physicochemical property that affects the optical properties and cloud condensation nuclei (CCN) activity. Multiple techniques are commonly employed to determine the aerosol mixing states for various applications, and comparisons between these techniques provide insights into the variations in aerosol chemical and physical properties. These techniques include size-resolved CCN activity measurements using a system with a CCN counter (CCNC) coupled with a differential mobility analyzer (DMA), a Humidified/Volatility Tandem Differential Mobility Analyzer (H/V-TDMA) that measures aerosol hygroscopicity and volatility distributions, and a single-particle soot photometer (SP2) that directly quantifies black carbon (BC) mixing states. This study provides the first comparison of aerosol mixing state parameters obtained through simultaneous measurements using DMA-CCNC, H/VTDMA, and DMA-SP2. The impacts of primary aerosol emissions and secondary aerosol (SA) formation on the aerosol mixing states and the intercomparison results were analyzed. The results showed that the differences in the mixing-state parameters measured using different techniques varied significantly under different conditions. The V-TDMA and DMA-SP2 measurements showed that the non-volatile population identified by V-TDMA was mainly contributed by the BC-containing aerosols. HTDMA and DMA-SP2 measurements indicated that a substantial proportion of nearly hydrophobic aerosols did not originate from BC-containing aerosols but likely originated from fossil fuel combustion and biomass-burning emissions. The synthesized comparison results between the DMA-CCNC, HTDMA, and DMA-SP2 measurements revealed that some nearly hydrophobic BC-free particles were CCN-inactive under supersaturated conditions, likely from fossil fuel combustion emissions. In contrast, others were CCN-active under supersaturated conditions linked to biomass-burning emissions. BC-containing aerosols emitted from fossil fuel combustion tend to be more externally mixed with other aerosol components than those emitted by biomass-burning activities. These results highlight significant disparities in the mixing states and physiochemical properties of aerosols from fossil fuel and biomass burning. The formation of secondary nitrate and organic aerosols significantly affects variations in aerosol mixing states, generally enhancing aerosol hygroscopicity and volatility while reducing differences in mixing state parameters derived from different techniques, reducing aerosol heterogeneity. Variations in the number of BC-free particle fractions showed that SAs tended to form more quickly on BC-free

particles than on BC-containing particles. Further comparison of the mixing state parameters revealed that the two resolved secondary organic aerosol factors in this study exhibited remarkably different physical properties, indicating that they likely formed through different pathways. These findings suggest that comparisons among aerosol mixing states derived from different techniques can provide deeper insights into the physical properties of aerosols and how they are affected by SA formation, aiding the investigation of SA formation pathways.

1 Introduction

The aerosol mixing state is a crucial physicochemical property of aerosol particles (Riemer et al., 2019), exerting a significant impact on their optical properties and cloud condensation nuclei (CCN) activity, thus affecting their impact on the climate and environment (Fierce et al., 2017; Riemer et al., 2019; Stevens et al., 2022). For example, variations in the mixing state of black carbon (BC) particles can significantly alter their absorption and radiative effects (Bond et al., 2013; Lack et al., 2012; Zhao et al., 2019; Moffet et al., 2016; Matsui et al., 2018; Peng et al., 2016). Using simple internal mixing state assumptions for aerosol chemical compositions to estimate CCN number concentrations can lead to substantial overestimations (up to 30%; Deng et al., 2013; Farmer et al., 2015; Ren et al., 2018; Ching et al., 2017, 2019; Tao et al., 2021). The aerosol mixing state varies widely due to complex emissions and atmospheric transformations, leading to significant uncertainties in estimating the effects of aerosols based on simplified mixing state assumptions (Ervens, 2015; Wang et al., 2022; Fu et al., 2022).

The aerosol mixing state describes the mixture of aerosol chemical components within each particle and the distribution of these particles in the aerosol population. This property can be directly measured using single-particle chemical composition techniques (Fierce et al., 2017; Riemer et al., 2019), such as the single-particle soot photometer (SP2), which measures refractory black carbon (rBC) mass concentrations and the mixing state of rBC with other aerosol components, or single-particle chemical composition measurement techniques (e.g., single-particle aerosol mass spectrometer, SP-AMS) that have been developed in recent years (Lee et al., 2019; Riemer et al., 2019 and reference therein). Alternatively, the aerosol mixing state can be inferred from indirect measurements of aerosol properties, such as size-resolved aerosol CCN activity (measured by coupling a differential mobility analyzer (DMA) and a CCN counter (CCNC)), size-resolved aerosol hygroscopicity distributions, or volatility distributions (measured by a Humidified/Volatility Tandem differential mobility analyzer (H/V-TDMA)).

However, each technique yields information on aerosol mixing states based on different aerosol microphysical properties, thus obtaining aerosol mixing states that are different but linked to one another. For instance, while both CCN activity and hygroscopic growth measurements are associated with aerosol hygroscopicity, an intercomparison between CCNC and HTDMA measurements has

prompted investigations into aerosol hygroscopicity variations under different saturation conditions (Su et al., 2010; Juranyi et al., 2013; Lance et al., 2013; Kawana et al., 2016; Tao et al., 2020; Jiang et al., 2021). Although the SP2 and VTDMA techniques depend on the evaporation of non-refractory compositions, only rBC remains in the SP2 measurements. In contrast, non-refractory composition evaporation depends on the thermodynamic temperature in the VTDMA measurements. Thus, measurements of an SP2 are highly correlated to those of a VTDMA at high temperatures (200 °C– 300 °C), with their differences reflecting variations in aerosol density, shape, or volatility (Philippin et al., 2004; Wehner et al., 2009; Adachi et al., 2018, 2019; Wang et al., 2022). HTDMA and VTDMA can be combined to study the influence of the aerosol mixing state on hygroscopicity and volatility (Zhang et al., 2016; Cai et al., 2017; Wang et al., 2017). Strong correlations were found between the hydrophobic and non-volatile particles, suggesting they might have similar chemical compositions (Zhang et al., 2016). In addition, some studies have shown that, except for BC, low-volatility particles correlate well with CCN-inactive particles based on VTDMA and CCNC measurements (Kuwata et al., 2007; Kuwata and Kondo, 2008; Rose et al., 2011; Cheng et al., 2012). Therefore, intercomparisons between mixing state parameters measured by distinct techniques provide a better characterization of the aerosol mixing state and insight into aerosol physiochemical properties. Previous studies have mainly compared two types of aerosol mixing state measurements and lacked a comprehensive comparative analysis among SP2, DMA-CCN, and HV-TDMA measurements, hindering the wide application of derived aerosol mixing states obtained by individual techniques.

The mixing state of primary aerosols can vary greatly depending on their type and emission conditions (Cheng et al., 2012; Wang et al., 2017; Wang et al., 2022; Ting et al., 2018; Liu et al., 2021) and can be significantly altered during aging processes or secondary formations (Wehner et al., 2009; Cheng et al., 2012; Wang et al., 2022; Tomlin et al., 2021; Lata et al., 2021). Primary aerosol emissions, such as biomass burning, fossil fuel combustion, and cooking, tend to contribute to weak hygroscopicity (Herich et al., 2008, 2009; Wang et al., 2020; Kim et al., 2020) and low-volatility aerosols (Hong et al., 2017; Saha et al., 2018). The formation of secondary aerosols (SAs), including the aging of BC-containing aerosols and primary organic aerosols, mainly contributes to aerosols with strong CCN activity (Mei et al., 2013; Ma et al., 2016; Tao et al., 2021) and high hygroscopicity (Chen et al., 2018; Kim et al., 2020; Wang et al., 2020). It is important to study the impact of specific primary

aerosol emissions and SA formation on aerosol mixing states and the influence of aerosol mixing state parameters derived from different techniques to enhance our understanding of the mixing state of aerosols from different emission sources and improve their characterization in models.

The North China Plain (NCP) is among the most polluted regions in China, with various primary emission sources and strong SA formations that play critical roles in air pollution (Xu et al., 2011; Tao et al., 2012; Liu et al., 2015). The complex mixing state of aerosols in the NCP contributes to uncertainties in evaluating their climate and environmental effects (Zhuang et al., 2013; Nordmann et al., 2014; Zhang et al., 2016; Tao et al., 2020; Shi et al., 2022), particularly regarding BC particles (Wu et al., 2017; Liu et al., 2019; Zhao et al., 2019; Wang et al., 2011; Zheng et al., 2019). Meteorological conditions can greatly affect SA formation in the NCP and can be significantly exacerbated during severe pollution events. SA formation under low relative humidity (RH) conditions, mainly through the condensation of gaseous-phase oxidation products, would change to that mainly occurring in the aqueous phase under high RH conditions (Kuang et al., 2020). Because SAs formed through different mechanisms, have different chemical compositions and add mass to different aerosol populations, SA formation under different meteorological conditions can affect the aerosol mixing states differently (Tao et al., 2021). This study obtained the aerosol mixing state through concurrent measurements of the CCN activity, hygroscopicity, volatility, and BC particles at a regional site in the NCP using CCNC, HTDMA, VTDMA, and SP2 instruments. This provides a unique opportunity to perform a comprehensive inter-comparison of the aerosol mixing states among different techniques to gain insight into the impact of primary aerosol emissions and SA formation on the observed aerosol mixing states.

2 Materials and methods

2.1 Campaign information and instruments setup

From the 16th of October to the 16th of November 2021, aerosol mixing states were continuously and concurrently monitored using different techniques at the Gucheng site in Dingxing County, Hebei Province, China, as part of a campaign to investigate AQueous Secondary aerosol formation in fog and aerosols and their radiative effects in the NCP (AQ-SOFAR). The observation site, located at 39°09'N, 115°44'E, is an Ecological and Agricultural Meteorology Station of the Chinese Academy

of Meteorological Sciences, situated between the megacities of Beijing (approximately 100 km away) and Baoding (approximately 40 km away) and surrounded by farmlands and small towns. This site provides a representative view of the background atmospheric pollution conditions in the NCP (Kuang et al., 2020; Li et al., 2021).

Different measurement techniques were used to simultaneously obtain the aerosol mixing state through CCN activity, hygroscopicity, volatility, and BC particle observations. In addition to aerosol mixing state measurements, the AQ-SOFAR campaign includes measurements of aerosol number size distribution, chemical composition, aerosol scattering, and absorption properties. Aerosol number size distributions in the diameter range of 13 nm–4 µm were measured by the scanning mobility particle sizer (13–550 nm) and the aerodynamic aerosol classifier (100 nm–4 µm), and they are merged by assuming an aerosol density of 1.6 g/cm^3. The total BC mass concentrations were determined using an aethalometer (Magee, AE33; Drinovec et al., 2015); more information on the correction of absorption measurements and mass concentration calculations is available in Luo et al. (2022). All aerosol measurement instruments were housed in a temperature-controlled container at 24 °C. The inlet was switched among three impactors: TSP (Total Suspended Particles), PM$_{2.5}$ (Particulate Matter with an aerodynamic diameter of less than 2.5 µm), and PM$_1$ (Particulate Matter with an aerodynamic diameter of less than 1 µm). Inlet changes among impactors affect dry-state aerosol sampling owing to ambient aerosols are enlarged through aerosol hygroscopic growth or activation. However, the aerosol mixing state and aerosol chemical composition measurements were made on submicron aerosols, and the inlet change almost did not affect those measurements under conditions of RH less than 90%. The sampled aerosol was dried by two parallelly assembled Nafion dryers with a length of 1.2 m. Two Nafion driers was used because of the high RH and sample flow rate (~16 L/min) during the campaign to ensure drying efficiency. In addition, during autumn and winter in the NCP, ambient air temperature (<20 °C and sometimes <0 °C) can be significantly lower than the room temperature (~24 °C). Therefore, this dryer system can maintain the RH of sampled aerosols to below 20%. Meteorological data such as temperature, pressure, wind speed, wind direction, and RH were obtained from an automatic weather station operated by the station.

The chemical composition of the submicron aerosols was analyzed using a High-Resolution Time-of-Flight Aerosol Mass Spectrometer (HR-ToF-AMS). The ionization efficiency (IE) was calibrated using 300 nm diameter pure NH$_4$NO$_3$ particles, following the standard protocols outlined in

Jayne et al. (2000) in the middle of the campaign, with the relative ionization efficiency (RIE) of ammonium determined to be 5.26. The RIE of sulfate was 1.28 using pure $(NH_4)_2SO_4$ particles, and the default RIEs of 1.4 for organic aerosols, 1.1 for nitrates, and 1.3 for chlorides were used as the organic aerosols. The composition-dependent collection efficiency reported by Middlebrook et al. (2012) was used. Elemental ratios were derived using the "Improved-Ambient (I-A)" method as described in Canagaratna et al. (2015), including hydrogen to carbon (H/C), oxygen to carbon (O/C), and organic mass to organic carbon (OM/OC) ratios. Two primary organic aerosol (POA) and two oxygenated organic aerosol (OOA) factors were identified by High-Resolution Positive Matrix Factorization (HR-PMF; Ulbrich et al., 2009; Paatero and Tapper, 1994). This study used the summation of the two OOA factors to represent secondary organic aerosols (SOA). The mass spectra of the organic aerosol (OA) factors and their correlations with external species are shown in Figs. S1 and S2. The Biomass Burning Organic Aerosol (BBOA) spectrum was characterized by obvious m/z 60 (mainly $C_2H_4O_2^+$) and 73 (mainly $C_3H_5O_2^+$), two indicators of biomass burning (Mohr et al., 2009). BBOA correlated well with $C_2H_4O_2^+$ (R^2=0.91) and $C_3H_5O_2^+$ (R^2=0.90). Consistent with previous studies in Beijing (Xu et al., 2019), the PMF analysis revealed a mixed factor named Fossil Fuel Organic Aerosol (FFOA), which comprises traffic emissions and coal combustion and is characterized by a typical hydrocarbon ion series. FFOA had a relatively high f_{44} (0.083) value, which was likely due to aging during regional transportation, similar to the results observed in the winter of 2016 in Beijing (Xu et al., 2019) and coal combustion organic aerosols in Gucheng (Chen et al., 2022). Secondary organic aerosol formation from volatile organic compound precursors could occur in different formation pathways, such as aqueous-phase, heterogeneous, or gas-phase reactions. It might also be oxidized under different conditions, such as oxidation under different nitrogen oxide conditions with different oxidation capacities and oxidants. The two resolved OOA factors displayed different spectral patterns, correlations with tracers, and diurnal variations, suggesting that they resulted from different chemical processes. However, their formation mechanisms remain to be explored in future studies. In general, the OOA factor 1 (OOA1) has higher $CO_2^+/C_2H_3O^+$ (3.9) and O/C (0.91) ratios than OOA factor 2 (OOA2) with 2.1 and 0.78, respectively.

This study did not consider losses in the inlet line and sampling systems for the following reasons: (1) investigated mixing state parameters are represented by number fractions (NFs) of

different diameters, which are much less affected by losses in sampling systems compared with absolute number concentrations; and (2) good consistency was achieved between measurements of particle number size distributions (PNSD) and mass concentrations measured by AMS. The average ratio between volume concentration derived from AMS and rBC measurements (densities of compounds are the same as Kuang et al., 2021) and the volume concentration derived from PNSD measurements was 0.79 (R=0.97, as shown in Fig. S3), consistent with previous reports as AMS cannot detect aerosol components, such as dust (Kuang et al., 2021).

2.2 Aerosol mixing states measurement techniques

2.2.1 DMA-CCNC measurements

The CCN activity of the particles under supersaturated conditions was measured using a DMA-CCNC system, which consisted of a differential mobility analyzer (DMA; model 3081, TSI, Inc., MN, USA), condensation particle counter (CPC; model 3756, TSI, Inc., MN, USA), and continuous-flow CCNC (model CCN100, Droplet Measurement Technologies, USA). The system was operated in size-scanning mode and provided the Size-resolved Particle Activation Ratio (SPAR) by combining CPC and CCNC measurements at different particle sizes. To compare the instruments, three supersaturations (SSs) of 0.08%, 0.14%, and 0.22% were applied in a single cycle of approximately 15 min. CCN measurements under these three SSs revealed that the CCN activity of aerosols resides in the accumulation mode with an aerosol diameter range of approximately 100–200 nm, which is close to the diameters of the HV-TDMA measurements. Higher SSs would reveal CCN activities of smaller aerosol particles (<100 nm), where the DMA-SP2 measurement is unavailable. The sample and sheath flow rates of DMA were set at 1 and 5 lpm, respectively, resulting in a measured particle diameter range of 9–500 nm, with a running time of 5 min per cycle. Supersaturation in the CCNC was calibrated with monodisperse ammonium sulfate particles (Rose et al., 2008) before and after the campaign. The flow rates were also calibrated before and after the campaign and checked daily to minimize uncertainties in droplet counting and supersaturation formed in the column (Roberts and Nenes, 2005; Lance et al., 2006). SPAR deviations due to multiple-charge particles were corrected using a modified algorithm based on Hagen and Alofs (1983) and Deng et al. (2011). Further details regarding this system can be found in Ma et al. (2016) and Tao et al. (2021).

2.2.2 H/V-TDMA measurements

The mixing state of the aerosols in terms of hygroscopicity and volatility was measured using a Hygroscopicity/Volatility Tandem Differential Mobility Analyzer (H/V-TDMA; Tan et al., 2013). The H/V-TDMA consisted of two DMA (Model 3081 L, TSI Inc.), with the first DMA (DMA1) selecting dried particles without conditioning (RH ~15%) and the second DMA (DMA2) selecting conditioned particles. H/V-TDMA can operate in either H- or V-mode, controlled by a three-way solenoid valve. A Nafion humidifier was used in the H-mode to condition the selected dry particles to 90% RH equilibrium. The number-size distribution of humidified particles (D_p) was measured using DMA2 and CPC (Model 3772, TSI Inc.). The RH-dependent hygroscopic growth factor (GF) at a specific diameter (D_d) was calculated as follows:

$$GF = \frac{D_p(RH)}{D_d} \qquad (1)$$

where $D_p(RH)$ is the size of particles undergoing humidification. Four dry electrical mobility diameters (50, 100, 150, and 200 nm) were measured in this mode. The instrument was regularly calibrated using standard polystyrene latex spheres (PSL) and ammonium sulfate particles.

In V-mode, a heated tube evaporated the volatile coatings from the previously selected dry particles. Six temperature settings were used for the heated tube, ranging from 25–200°C. The number-size distributions of the heated particles were measured using DMA2 and CPC. In addition to the four particle sizes measured in the H-mode, three additional particle sizes (250, 300, and 350 nm) were measured in the V-mode (residence time inside the heated tube to be about 1.6 s; Hong et al., 2017). The temperature-dependent shrinkage factor (SF), which is the ratio of heated particle size to dry particle size without heating (D_d), is defined as:

$$SF = \frac{D_p(T)}{D_d} \qquad (2)$$

where $D_p(T)$ denotes the particle diameter during heating. A complete cycle of H-mode measurements under one RH condition and V-mode measurements at six temperatures took approximately 3 h. The Probability Density Function (PDF) of the GF (or SF) was calculated from the measured density function using the inversion algorithm described by Stolzenburg and McMurry (2008).

2.2.3 DMA-SP2 measurements

The size-resolved BC mixing states were measured using an SP2 (Droplet Measurement Technology, Inc., USA) after DMA (Model 3081, TSI, USA). The DMA selected aerosols of various dry particle sizes, which were then introduced into SP2. The DMA-SP2 setup was able to measure the mixing states of aerosols with diameters (detection limit of approximately 80 nm based on the calibration) of 100, 120, 160, 200, 235, 270, 300, 335, 370, 400, 435, 470, 500, 535, 570, 600, 635, 670, and 700 nm within 20 min when it was not placed after an enuder-bypass switch system (the 13th to the 24th of October, 09:00 am of the 5th of November to 09:00 am of the 8th of November). However, it only measured mixing states at diameters of 120, 160, 200, 250, 300, 400, and 500 nm when it was placed after a thermodenuder-bypass switch system (11:00 am of the 24th of October to 08:00 am of the 5th of November, and 09:00 am of the 8th of November to 06:00 pm of the 17th of November). Because the HTDMA and VTDMA measurements were conducted solely by a single H/VTDMA system operating in different modes, the time needed for a single particle size measurement of HTDMA and VTDMA was much longer than that of the DMA-SP2 system. Thus, more particle sizes were selected in the DMA-SP2 system for acquiring the BC mass concentration and mixing state at larger diameters than HTDMA and VTDMA.

The SP2 chamber had a continuous Nd:YAG laser beam with a wavelength of 1064 nm. The BC-containing particles passing through the laser beam became incandescent by absorbing radiation. The mass concentration of the BC was calculated by measuring the intensity of the emitted incandescent light. The sheath flow/sample flow ratio was maintained at 10 for the DMA to reduce the width of the diameter distribution of the selected monodisperse aerosols. Additionally, the flow rate of the SP2 was changed from 0.1 to 0.12 L/min starting on the 22nd of October (allowed flow rate range of SP2: 0.03–0.18 L/min from the specification). SP2 was calibrated using quadag soot particles, as reported by Gysel et al. (2011). Further details regarding the calibrations are provided in Section 1 of the Supplementary Information.

2.3 Derivations of mixing state parameters

2.3.1 Fitting SPAR curves measured by the DMA-CCNC system

The SPAR curves were parameterized using a sigmoidal function with three parameters. As shown in Fig. S4, a sigmoidal curve generally characterized the measured SPAR. This parameterization assumes that the aerosol is an external mixture of CCN-active hydrophilic and CCN-

11

289   inactive hydrophobic particles (Rose et al., 2010). The formula used to parameterize the SPAR ($R_a(D_d)$)

290   for a specific SS is as follows (Rose et al., 2008):

291    $$R_a(D_d) = \frac{MAF}{2}\left(1 + erf\left(\frac{D_d - D_a}{\sqrt{2\pi}\sigma}\right)\right)$$ (7)

292   where erf denotes the error function. The Maximum Activation Fraction (MAF) is an asymptote of the

293   measured SPAR curve for large particles, as shown in Fig. S4, representing the fraction of CCNs

294   relative to the total number of particles. D_a is the midpoint activation diameter, is linked to the

295   hygroscopicity of the CCNs, and indicates the diameter where the SPAR equals half of the MAF value.

296   The σ is the standard deviation of the cumulative Gaussian distribution function and characterizes the

297   heterogeneity of CCN hygroscopicity. In Fig. S4, the σ indicates the slope of the steep increase in the

298   SPAR curves when the diameter is close to Da. Generally, hydrophilic particles larger than D_a can

299   become CCN. Therefore, these three parameters can be used to characterize the hygroscopicity of these

300   hydrophilic particles. This study did not consider the impact of nearly hydrophobic particles on SPAR,

301   as deviations from this parameterization scheme due to this impact were negligible at low SSs, as

302   stated in Tao et al. (2020).

303

304   **2.3.2 Classification of particle type based on hygroscopicity or volatility**

305   In this study, ambient aerosol particles were classified into two groups based on their

306   hygroscopicity (hydrophobic and hydrophilic) and two groups based on their volatility (non-volatile

307   and volatile) based on the measurements from H/V-TDMA (Wehner et al., 2009; Liu et al., 2011;

308   Zhang et al., 2016). Each group can be defined using the critical values of GF or SF as follows:

309   hydrophobic population: $GF < GF_C$; hydrophilic population: $GF \geq GF_C$; non-volatile population: $SF \geq SF_C$;

310   and volatile population: $SF < SF_C$.

311   The critical values of GF (GF_C) and SF (SF_C) in H/V-TDMA depend on the particle size and

312   working conditions, such as relative humidity and heating temperature. During this campaign, the SF_C

313   was set to 0.85 for all seven measured particle sizes at a temperature of 200 °C. The GF_C for the four

314   measured particle sizes of 50, 100, 150, and 200 nm were 1.1, 1.15, 1.175, and 1.2, respectively, and

315   the corresponding hygroscopicity parameter, κ, was approximately 0.07. These values of GF_C and SF_C

316   divide the probability density functions (PDFs) of SF and GF into two modes, consistent with prior

317 NCP studies (Liu et al., 2011; Zhang et al., 2016). The NF for the hydrophilic group (NF$_H$) and volatile

318 group (NF$_V$) can be calculated as follows:

$$NF_H = \int_{GF_C}^{\infty} GFPDF(GF)dGF \qquad (7)$$

319

$$NF_V = \int_0^{SF_C} SFPDF(SF)dSF \qquad (8)$$

320

321 where GFPDF and SFPDF are the PDFs of GF and SF, respectively, derived from H/V-TDMA

322 measurements.

2.3.3 Classification of particle type based on DMA-SP2 measurements

324 BC-containing aerosols can be categorized into two groups based on coating thickness: bare

325 BC/thinly coated BC particles and thickly coated BC particles. For the measurement of coated BC

326 particles at SP2, the incandescence signal is generally detected later than the scattering signals and the

327 time difference between the occurrence of the peaks of the incandescence and scattering signals is

328 defined as the lag time (Moteki & Kondo, 2007; Sedlacek et al., 2012; Subramanian et al., 2010). The

329 coating thickness of BC-containing aerosols in the SP2 measurement can be indicated by the lag time

330 (Moteki and Kondo, 2007; Schwarz et al., 2006; Sedlacek et al., 2012; Subramanian et al., 2010;

331 Metcalf et al., 2012), which has exhibited a clear two-mode distribution in previous studies (Zhang et

332 al., 2018; Zhao et al., 2021). A critical lag time threshold can be used to differentiate between the

333 different types of BC-containing aerosols and calculate the NF of bare and coated BC particles in the

334 total identified aerosols. In this study, a two-mode distribution of the lag time (Δt) was observed, and

335 a critical value of 0.8 μs was used to classify the BC-containing particles into thinly coated (or bare)

336 BC (Δt<0.8 μs) and thickly coated BC (Δt$\geqslant$0.8 μs). The definitions of all abbreviations are listed in

337 Table 1.

3 Results and discussions

3.1 Campaign overview

340 The time series of the meteorological parameters, aerosol mixing state measurements using

341 different techniques, and mass concentrations of the aerosol chemical compositions are shown in Fig.

342 1. In detail, the measurements of aerosol mixing states include SPAR at an SS of 0.08% by DMA-

CCNC, GF-PDF (PDF of GF) at 200 nm by HTDMA, SF-PDF (PDF of SF) at 200 nm and 200 °C by VTDMA, and lag time PDF of 200 nm BC-containing particles by DMA-SP2. The SIA, SOA, POA, and BC mass concentrations are shown in Fig. 1（b）. Three periods with significantly different aerosol pollution conditions were identified during the campaign. As shown in Fig. 1(b), before the 23rd of October (moderately polluted period), the accumulation of aerosols led to SIA mass concentrations <20 µg/m^3. In contrast, the highest mass concentrations of SOA, POA, and BC reached beyond 10 µg/m^3. The mass concentrations of different aerosol components increased significantly from the 23rd of October to the 6th of November (heavily polluted period with an average non-refractory PM$_1$ mass concentration of 49.5±22.5 µg/m^3) and decreased to much lower levels after the 6th of November (clean period with a non-refractory PM$_1$ mass concentration of 5.1±3.3 µg/m^3). Two particle groups were identified concerning the CCN activity, hygroscopicity, volatility, and coating thickness, as demonstrated by the SPAR, GF-PDF, SF-PDF, and lag-time PDF of BC-containing particles. Significant variations in the aerosol mixing states were also observed during the three periods with different pollution conditions, as demonstrated by the variations in SF-PDF measured by VTDMA. For example, the SF of the non-volatile particle group decreased during the heavily polluted period. Aerosol mixing states may have changed because of various transformations in existing aerosol particles and distinct secondary formation processes under different pollution conditions (Kuang et al., 2020; Tao et al., 2021; Shi et al., 2022; Yang et al., 2022). Diurnal variations in the mass concentrations of different aerosol chemical components and mixing states can be observed in the variations in the SPAR measurements, as previously observed in this region (Liu et al., 2011; Ma et al., 2012; Kuang et al., 2015; Tao et al., 2020).

Fig. 2 shows the campaign-averaged SPAR at the three SSs, PDF of the lag time of BC-containing particles, GFPDF, and SFPDF at 200 °C for different particle sizes. The sigmoidal SPAR curves were characterized by a rapid increase, followed by a gradual increase to unit 1, similar to the measured SPAR curves previously observed in this region (Deng et al., 2011; Zhang et al., 2014; Ma et al., 2016; Tao et al., 2018). At lower SSs, the particle size required for CCN activation was larger; thus, rapid increases in the SPAR curves occurred at larger particle sizes. In addition, the maximum AR of the SPAR curves decreases as fewer particles are CCN-active under low SSs. For the three measured SSs, the particle sizes where SPAR equals approximately 0.5 are approximately 90, 120, and 180 nm for

the three SSs of 0.08%, 0.14%, and 0.22%, respectively, consistent with the average D_a (see Eq. 7) values of the campaign. The NF of CCN-active particles in large-diameter ranges (which varies with SS and, for example, is greater than 200 nm for 0.08%) can be indicated by the gradual increase in the SPAR curves and quantified by the fitting parameter, MAF (see Eq. 7). The PDFs of the lag time, GF, and SF were all characterized by a bimodal distribution, which indicates two particle groups of BC-containing aerosols with different coating thicknesses, hygroscopicity, and volatility. The variations in the aerosol mixing states were further analyzed based on the measured mixing state parameters.

3.2 Intercomparisons among aerosol mixing state parameters derived using four techniques

The size-dependent characteristics of the aerosol mixing state parameters derived from the measurements of the four techniques and the MFs of different aerosol chemical compositions during the three pollution periods are shown in Fig. 3. In general, the size-dependent characteristics of MAF, NF_H, NF_V, and NF_{noBC} were similar, suggesting that they were likely dominated by the same particle group, namely BC-free particles. This particle group had the highest fraction (>0.7) during the heavily polluted period and the lowest fraction (down to 0.5) during the clean period, with the fraction decreasing with increasing particle size. This suggests that primary emissions tend to have higher fractions of BC-containing particles in larger diameter ranges; for example, the fraction of BC-containing particles increases from ~0.1 to ~0.4 as the particle size increases from 200 to 500 nm during the cleaning period. Because the bulk aerosol MF is mostly contributed by particles >300 nm, there may have been more hydrophilic, volatile, CCN-active, and BC-free particles with larger sizes (>300 nm) during the heavily polluted period owing to strong SA formation in larger diameter ranges (Kuang et al., 2020), resulting in a higher NF of these particles compared to the clean period. As for R_{exBC}, the small size dependence of R_{exBC} during the moderately polluted period might have been associated with stronger primary emissions, while the decrease in R_{exBC} with increasing particle diameter in the polluted period confirmed that SA formation is more efficient for particles with larger diameters.

As for the difference among the aerosol mixing state parameters, NF_V and NF_{noBC} agreed with each other with a <0.1 difference, and both were higher than NF_H by at least 0.1 NF_H in the moderately polluted period. Compared with NF_{noBC}, NF_V was higher during the heavily polluted period, when the nitrate fraction was the highest (~30%). The SOA fraction was the lowest (~7%) among all three

periods, suggesting that some BC-containing aerosols in this period were also identified as volatile, consistent with the fact that the formation of semi-volatile nitrate in BC-containing particles increases their volatility. However, during the cleaning period, NF_V was even lower than NF_{noBC}, suggesting that some BC-free aerosols were characterized as low volatile and non-negligible fractions of BC-free aerosols dominated these less volatile aerosol components, which were likely less volatile organic aerosols (not likely contributed by BC-containing particles with a BC smaller than the SP2 detection limit, because the SF of this type of volatile BC-containing aerosols has an SF lower than 80/200, which is substantially lower than the threshold SF of 0.85 for NF_V calculation). In addition, the MAF values generally agreed with the NF_H during the clean period. However, they were larger than the NF_H during the moderately and heavily polluted periods (by ~0.2) when the POA/SOA fractions were higher (~40% vs. ~35%). POA generally has a lower hygroscopicity than SOA. The critical κ of hydrophilic mode aerosols was 0.07, suggesting that a higher fraction of aerosols had κ below 0.07 (i.e., hydrophobic mode aerosols in this study) during the moderately polluted period. However, under supersaturated conditions, they demonstrate enhanced hygroscopicity by becoming CCN-active. NF_H was consistently lower than NF_V and NF_{noBC} (the average difference between NF_H and NF_{noBC} was approximately 0.2). As mentioned above, NF_H was also lower than MAF during moderately polluted periods, and there may be a significant fraction of volatile BC-free aerosols with hygroscopicity lower than the critical κ value of 0.07; however, they were still CCN-active and therefore not fully hydrophobic.

The diurnal variations in MAF, NF_H, NF_V, and NF_{noBC}, along with the MFs of the aerosol chemical components during the three periods, are shown in Fig. 4. Except for a particle size of 50 nm, the diurnal variations in these four mixing state parameters were generally similar for all measured sizes. The different diurnal variations at a particle size of 50 nm may be due to the different effects of emissions and aging processes on the different aerosol modes, as particles <100 nm mainly reside in the Aitken mode, which is where particles >100 nm mainly reside in the accumulation mode (Wang et al., 2022). For particles >100 nm (Fig. 4 and S5), there was a maximum in the afternoon for MAF, NF_H, NF_V, and NF_{noBC}, indicating a peak during this time due to an increase in SA compositions, such as nitrate and SOA, and a decrease in POA and BC. Diurnal variations in the aerosol mixing state parameters and chemical compositions were more pronounced during the moderately polluted period.

During heavily polluted periods, the diurnal variation was least pronounced for NF_V and most pronounced for NF_H. In the clean-air period, there was another maximum at midnight for MAF and NF_{noBC}, which may be attributed to the diurnal variations in SA compositions, such as sulfate and SOA, and the decrease in BC and FFOA. The average-size dependence of the aerosol mixing state parameters over different time ranges during a heavily polluted period is shown in Fig. S6. It can be seen that the differences among the four parameters were the least from 12:00 to 18:00, with the most SOA and the least POA. This is consistent with the results shown in Fig. 3, where the difference between the MAF and NF_H decreased when the POA fractions were the smallest. R_{exBC} tended to be lower during the daytime, and its diurnal variation was more significant for larger particle sizes. In general, the diurnal variations for R_{exBC} were opposite to those of NF_{noBC} and agreed better with those of the primary aerosol MFs. This is because BC particles originate from primary emissions and are mainly mixed externally. After aging in the atmosphere, BC particles can be coated by SAs, resulting in more coated BC particles and fewer externally mixed BC particles. As SAs tend to form on larger particles, the diurnal variations in SA formation may significantly affect the RexBC of larger particle sizes.

As summarized in Table. S1, the comparison among MAF, NFH, NFV, and NFnoBC was conducted based on their correlations with different particle sizes. Note that the MAF at SSs of 0.08%, 0.14%, and 0.22% were used for comparison at 200, 150, and 100 nm particle sizes. This is because the diameter range of rapid increases in the SPAR curves is determined by aerosol hygroscopicity in this particle size range. The midpoints of the rapidly increasing diameter ranges of the SPAR curves at SSs of 0.08%, 0.14%, and 0.22% were approximately 180 nm, 120 nm, and 90 nm, respectively (as shown in Fig. 2). In general, there were moderate correlations (r=~0.5) between MAF, NF_H, and NF_V, suggesting that a similar particle group contributed to the dominance of CCN-active, hygroscopic, and volatile aerosols (Zhang et al., 2016). The agreement between MAF and NF_V was slightly higher than that between MAF and NF_H or between NF_H and NF_V with similar correlation coefficients (~0.65). However, smaller systematic differences (slope and intercept) were much closer to 1 and 0, respectively. This is consistent with the previous finding that a substantial fraction of volatile but less hygroscopic aerosols are CCN-active. For smaller particle sizes, the correlation became weaker (r=~0.4), whereas the degree of reduction was the lowest for the correlation between MAF and NF_V.

3.3 Impacts of primary aerosol emissions on aerosol mixing states and parameter intercomparisons

Fig. 5 presents the correlation between each aerosol mixing state parameter at 200 nm and the MF of each primary organic aerosol composition during the three periods. The four mixing state parameters (MAF, NF_H, NF_V, and NF_{noBC}) were negatively correlated with MF_{FFOA} and MF_{BBOA}. However, the anticorrelation with MF_{FFOA} (-0.45~-0.74) was much stronger than MF_{BBOA} (-0.10~-0.45). Biomass-burning emissions and fossil fuel emissions are the two major sources of BC in the NCP (Yang et al., 2022), and NF_{noBC} was negatively correlated with MF_{FFOA} (r=-0.49) and weakly correlated (r=-0.18) with MF_{BBOA}, suggesting that fossil fuel emissions were likely the dominant source of BC during this field campaign. The negative correlation between MAF and MF_{FFOA} was weaker than that of NF_{noBC} with MF_{FFOA} (-0.62 vs. -0.49). In particular, at the same MF_{FFOA}, the MAF was lower than NF_{noBC}, demonstrating that some BC-free particles were CCN-inactive and were likely mainly composed of organic aerosols from fossil fuel combustion emissions. The negative correlation between NF_V and MF_{FFOA} was slightly weaker than between NF_{noBC} and MF_{FFOA} (-0.56 vs. -0.49). At the same MF_{FFOA}, NF_{noBC} was close to NF_V, and considering that BC-containing aerosols were dominated by thinly coated BC most of the time (Fig. 5), this demonstrates that the non-volatile population identified by V-TDMA was mainly contributed by BC-containing aerosols. NF_H had the lowest negative correlation with MF_{FFOA} (r=-0.74), demonstrating significant contributions from fossil fuel emissions to nearly hydrophobic aerosol populations. At the same MF_{FFOA}, NF_H was obviously lower than NF_{noBC} (NF_H and NF_{noBC} were larger and smaller than 0.7 when MF_{FFOA} was larger than 0.1), demonstrating that a substantial portion of nearly hydrophobic aerosols was not contributed by BC-containing aerosols (BC-containing aerosols of 200 nm with BC core smaller than 80 nm which is smaller than the detection limit of SP2 likely to be quite aged in the air, thus not possible to be nearly hydrophobic), but likely by FFOA- or BBOA-dominant aerosols (NF_H also had a negative correlation with MF_{BBOA}). However, the markedly different correlations between MAF and MF_{FFOA} (r=-0.62) and between MAF and MF_{BBOA} (r=-0.2) imply that nearly hydrophobic but CCN-active aerosols were likely contributed by biomass-burning emissions. The correlations between the ratio of thinly coated BC in the total BC-containing particles (R_{exBC}) and the MFs of BBOA and FFOA are shown in Fig. 6. Weak correlations (r<0.3) between R_{exBC} and MF_{BBOA} and MF_{FFOA} were observed. However, R_{exBC}

tended to increase with MF_{FFOA}, suggesting that BC-containing aerosols emitted from fossil fuel combustion tended to be more externally mixed with other aerosol components than those emitted from biomass burning. These results demonstrate remarkably different mixing states and the physical and chemical properties of fossil fuel combustion and biomass-burning aerosols.

The impact of primary emissions on the differences among the four aerosol mixing state parameters at a particle size of 200 nm was analyzed and is shown in Fig. 7. The difference between NF_{noBC} and NF_H (NF_{noBC}-NF_H) was significantly positively correlated with MF_{FFOA} and MF_{BBOA} (r>0.5), suggesting that a substantial proportion of POA resided in BC-free aerosols and was volatile, but contributed substantially to nearly hydrophobic aerosols; as did the differences between NF_V and NF_H (NF_V-NF_H). The MFs of BBOA and FFOA were poorly correlated with the differences between the MAF and NF_V (MAF-NF_V), MAF and NF_{noBC} (MAF-NF_{noBC}), and NF_V and NF_{noBC} (NF_V-NF_{noBC}) (Fig. S7). The difference between MAF-NF_H was positively correlated with MF_{BBOA}, further suggesting that BBOA contributed to nearly hydrophobic aerosols under subsaturated conditions; however, their hygroscopicity was enhanced, and they became CCN-active under supersaturated conditions. The correlations between the mixing-state parameters and primary aerosol composition during the campaign and different pollution periods are summarized in Fig. S7.

3.4 Impacts of SA formation on aerosol mixing states and parameter intercomparisons

The correlations between the aerosol mixing state parameters at 200 nm and the MF of each SA component are presented in Fig. 8 for three periods, and the entire campaign is presented. The analysis is conducted at only 200 nm, where all four aerosol mixing state parameters were measured to compare the four aerosol mixing state parameters and their relationships with aerosol chemical compositions simultaneously. Generally, MAF, NF_H, NF_V, and NF_{noBC} exhibited strong positive correlations with MF_{NH4} (r>0.5). This is likely because ammonium was mainly formed through neutralizing sulfuric and nitric acids with ammonia; therefore, variations in ammonium better represent overall secondary inorganic aerosol formation. As shown in Fig. 3, the secondary inorganic aerosol components dominated over SA (approximately 50% vs. approximately 70%), indicating that SA formation was primarily composed of secondary inorganic aerosol formation, which explains the weaker correlation with SOA (r=~0.3), as shown in Fig. 8.

During the clean-air period, when the MFs of SOA and sulfate were both above 15%, all four parameters had a strong positive correlation with MF_{SO4} and MF_{SOA} (r>0.5), suggesting that when a clean background air mass with higher fractions of sulfate and SOA prevailed, the local primary emissions that contributed substantially to BC-containing and less hygroscopic POA aerosols became less significant. The positive correlations between the MAF and SA components have been extensively discussed by Tao et al. (2021), who found that SA formation enhances the hygroscopicity of nearly hydrophobic aerosols, thereby increasing CCN activity. This also explains the strong correlation between the NF_H or MAF and ammonium formation. The strong positive correlations between NF_V and SA formation (r=~0.6) are consistent with the fact that nitrate dominates SA formation during this campaign and is semi-volatile. For the first time, strong positive correlations between NF_{noBC} and SA formation were observed (r=0.6). NF_{noBC} depends primarily on the relative variation between BC-containing and BC-free aerosols. The increase in NF_{noBC} at 200 nm as a function of the SA MF suggests that SAs migrated to a higher fraction of BC-free aerosols smaller than 200 nm to particle size of 200 nm, highlighting that SAs tended to form more quickly on BC-free aerosols than on BC-containing aerosols.

The effects of SA formation on the differences between the four aerosol mixing state parameters were studied and are illustrated in Fig. 9. The two OOA factors (OOA1 and OOA2) were formed through different chemical pathways. The difference between NF_{noBC} and NF_H (NF_{noBC}-NF_H) showed a strong negative correlation with MF_{NH4} and MF_{NO3} (mainly -0.6), as did the differences between NF_V and NF_H (NF_V-NF_H). As previously noted, NF_H typically has smaller values than NF_V and NF_{noBC}. Thus, a negative correlation between the MFs of ammonium and nitrate indicated that the formation of secondary nitrate resulted in a smaller difference between these mixing state parameters. An increase in the fraction of ammonium nitrate, a pure-scattering semi-volatile compound with strong hygroscopicity, can render the aerosol population more dominated by particles with strong volatility and hygroscopicity. As the secondary inorganic aerosol components increase, this can result in a smaller difference between NFnoBC, NFH, and NFV.

Furthermore, the difference between NF_V and NF_H showed a positive correlation with MF_{OOA2} and a negative correlation with MF_{OOA1}, indicating different volatility and hygroscopicity of the two SOA factors. The differences between NF_V and NF_H concerning the MF of OOA1 and OOA2 are

shown in Fig. 9(e) and (f), respectively. As previously noted, NF_V was generally higher than NF_H, and the difference between the two decreased with increasing MF_{OOA1}, which was generally smaller than 0.3. This suggests that the formation of OOA1 enhances the hygroscopicity of volatile particles, which aligns with the highest oxidation state of OOA1 (higher O/C but lower H/C compared to OOA2) and has a significant and overall positive impact on aerosol hygroscopicity (Cerully et al., 2015; Thalman et al., 2017; Zhang et al., 2023). A positive correlation was observed between NF_V and MF_{OOA2} (r=~0.25).

In contrast, the correlation between NF_H and MF_{OOA2} was weak (R was close to 0), implying that OOA2 might be semi-volatile but only weakly hygroscopic, which could contribute to NF_V being higher than NF_H as OOA1 increases. The difference between NF_{noBC} and NF_V ($NF_{noBC}-NF_V$) was negatively correlated with MF_{NO3}, which is consistent with the semi-volatile nature of nitrate. The negative correlation between $NF_{noBC}-NF_V$ and MF_{OOA2} indicates that the difference is smaller when there is more OOA2, implying that OOA2 is also a semi-volatile compound and is likely formed mainly on BC-free particles. The correlations between the differences between NF_V-MAF and NF_{noBC}-MAF and the MF of each SA composition were very weak. The impacts of SA formation on BC mixing states are shown in Fig. S8. In general, the NF of thinly coated BC has a negative correlation with SIA and a weak association with SOA, suggesting that SIA formation mainly enhances the thickness of the BC coating. The correlations between the mixing state parameters and SA composition during the campaign and different pollution periods are summarized in Fig. S9.

In addition to changes in the MFs of SA compositions, the accumulation of SA pollution may provide insights into the impact of SA formation on aerosol mixing states. As shown in Fig. 10(a), during the heavily polluted periods, there were two distinct pollution accumulation processes from the 23rd to the 27th of October and from the 28th to the 31st of October, respectively. During the pollution accumulation process, the mass concentration of SAs increased by approximately three-fold, indicating the rapid formation of secondary compositions and a significant increase in non-refractory PM_1 (NR-PM_1) mass concentration. Fig. 10(b) and (c) illustrate that this increase in SAs significantly enhanced aerosol mixing state parameters, including MAF, NF_V, NF_H, and NF_{noBC}, which increased from approximately 0.5 to 0.8 with evident diurnal variations. This highlights the impact of SA formation on the aerosol mixing states and the importance of studying the pollution accumulation processes of

SAs. The enhancements in the different aerosol mixing state parameters during the pollution accumulation process were not uniform. MAF and NF_H initially exhibited lower values than NF_V and NF_{noBC}; however, their later enhancement was stronger than that of NF_{noBC}. Fig. 10(d) and (e) show the difference between NF_{noBC} and NF_V at 200 and 300 nm as a function of SA mass concentrations during these two pollution periods, which clearly shows how, during SA formation, NF_V became higher than NF_{noBC} while NF_V remained close to the NF of thickly coated BC-containing aerosols (NF_{CBC}) plus NF_{noBC} ($NF_{CBC}+NF_{CBC}$). These results suggest that SA formation increases the volatility of BC-free and BC-containing aerosols, leading to an increased NF_V compared with NF_{noBC}. Almost all BC-free particles and some BC-containing aerosols become volatile during the accumulation of pollution.

4. Conclusions

The aerosol mixing state is one of the most important physicochemical properties of aerosol particles and significantly affects their optical properties and the CCN activity of aerosol particles. The aerosol mixing states vary significantly with complex aerosol emissions and atmospheric transformations. In this study, aerosol mixing states derived from CCN activity, hygroscopicity, volatility, and BC particle observations, along with their relationship to primary aerosol emissions and SA formation, were systematically analyzed based on simultaneous measurements of CCNC, H/VTDMA, and SP2. Statistical analysis demonstrated that the NFs of CCN-active, hygroscopic, and volatile particles were generally positively correlated and mainly contributed by BC-free aerosols. Therefore, four mixing state parameters were all negatively correlated to either the MFs of BBOA or FFOA because fossil fuel combustion and biomass burning were the two major sources of BC-containing aerosols during this field campaign. However, the differences between these mixing state parameters vary significantly under different conditions.

The intercomparison results highlight the differences in the aerosol mixing states and physicochemical properties caused by fossil fuel combustion and biomass-burning emissions. The CCN and SP2 measurements showed that CCN-inactive BC-free particles were mainly produced by fossil fuel combustion. In contrast, a comparison between the VTDMA and SP2 measurements indicated that the non-volatile aerosols mostly comprised BC-containing particles. The comparison

between HTDMA and SP2 measurements revealed that a significant proportion of nearly hydrophobic aerosols was not from BC-containing particles but from fossil fuel combustion or biomass-burning-dominated organic aerosols. The correlation between the CCNC and HTDMA measurements also showed that nearly hydrophobic, BC-free aerosols could become CCN-active under supersaturated conditions and are tightly linked to biomass-burning emissions. This suggests that biomass-burning aerosols may exhibit different hygroscopicities under sub- and supersaturated conditions (Bougiatioti et al., 2016). Furthermore, the correlation analysis between SP2 measurements and the MFs of BBOA and FFOA indicated that BC-containing aerosols from fossil fuel combustion tended to be more externally mixed with other aerosol compositions than those from biomass burning activities.

In addition to primary aerosol emissions, SA formation also significantly impacts variations in aerosol mixing states. During this campaign, SA formation was dominated by nitrate and SOA production, which had markedly different impacts on the aerosol mixing states owing to their different physical properties and formation pathways. NF_{noBC}, MAF, NF_H, and NF_V were all positively correlated with the nitrate and SOA MFs, revealing much stronger correlations with SOA than nitrate. This is consistent with the semi-volatile but highly hygroscopic properties of nitrates. The high correlation coefficient between NF_{noBC} and the MFs of SAs at 200 and 300 nm suggests that SA formation led to the migration of BC-free aerosols towards larger diameters more quickly than that of BC-containing aerosols. This result reveals that SAs formed more rapidly on BC-free than on BC-containing aerosols, which aligns with the hydrophobic nature of BC-containing aerosols that do not favor aqueous SA formation. Moreover, as the MFs of nitrate or ammonium increased, the differences between the mixing-state parameters (NF_{noBC}, MAF, NF_H, and NF_V) decreased because of the hygroscopic and semi-volatile nature of ammonium nitrate. However, the two resolved SOA factors exhibited different impacts on the differences between NF_V and NF_H (NF_V-NF_H), and their correlations with NF_V and NF_H revealed that OOA1 was more hygroscopic but less volatile, suggesting distinct formation mechanisms for these two OOA factors during the field campaign.

The findings of this study highlight the markedly different effects of primary emissions and SA formation on aerosol mixing states and suggest that comparisons of aerosol mixing states obtained using various techniques are useful for gaining insights into the hygroscopicity, volatility, and CCN activity of different aerosols. These comparisons also indicate the impact of SA formation on aerosol

632 physical properties, which can help understand the pathways of SA formation. However, it is important

633 to be cautious in the application of aerosol mixing state parameters because the suitability of VTDMA-

634 derived mixing state parameters for representing BC mixing states is largely dependent on the

635 composition and mass of the SAs.

636

639   **Competing interests**. The authors declare that they have no conflict of interest.

640

641   **Author Contributions**.

642   YK and WY planned this campaign and YK designed the aerosol experiments and conceived this

643   research together with JC, and JC wrote the manuscript. JC performed measurements of CCNC, BL

644   performed measurements of SP2 and analyzed SP2 datasets with the help of GZ, WQ and YL

645   performed AMS measurements, LL performed HV-TDMA measurements and conducted post-data

646   processing as well as some of data analysis. BX, HX, MMZ, HZ and SR participated this campaign

647   and helped instruments maintenance. GZ provided full support for the campaign. All authors

648   contributed to discussions and revisions of this paper.

654

References

Adachi, K., Sedlacek, A. J., Kleinman, L., Chand, D., Hubbe, J. M., and Buseck, P. R.: Volume changes upon heating of aerosol particles from biomass burning using transmission electron microscopy, Aerosol Science and Technology, 52, 46–56, https://doi.org/10.1080/02786826.2017.1373181, 2018.

Adachi, K., Sedlacek, A. J., Kleinman, L., Springston, S. R., Wang, J., Chand, D., Hubbe, J. M., Shilling, J. E., Onasch, T. B., Kinase, T., Sakata, K., Takahashi, Y., and Buseck, P. R.: Spherical tarball particles form through rapid chemical and physical changes of organic matter in biomass-burning smoke, Proceedings of the National Academy of Sciences, 116, 19336–19341, https://doi.org/10.1073/pnas.1900129116, 2019.

Bond, T. C., Doherty, S. J., Fahey, D. W., Forster, P. M., Berntsen, T., DeAngelo, B. J., Flanner, M. G., Ghan, S., Kaercher, B., Koch, D., Kinne, S., Kondo, Y., Quinn, P. K., Sarofim, M. C., Schultz, M. G., Schulz, M., Venkataraman, C., Zhang, H., Zhang, S., Bellouin, N., Guttikunda, S. K., Hopke, P. K., Jacobson, M. Z., Kaiser, J. W., Klimont, Z., Lohmann, U., Schwarz, J. P., Shindell, D., Storelvmo, T., Warren, S. G., and Zender, C. S.: Bounding the role of black carbon in the climate system: A scientific assessment, Journal of Geophysical Research-Atmospheres, 118, 5380–5552, https://doi.org/10.1002/jgrd.50171, 2013.

Bougiatioti, A., Bezantakos, S., Stavroulas, I., Kalivitis, N., Kokkalis, P., Biskos, G., Mihalopoulos, N., Papayannis, A., and Nenes, A.: Biomass-burning impact on CCN number, hygroscopicity and cloud formation during summertime in the eastern Mediterranean, Atmos. Chem. Phys., 16, 7389–7409, https://doi.org/10.5194/acp-16-7389-2016, 2016.

Cai, M., Tan, H., Chan, C. K., Mochida, M., Hatakeyama, S., Kondo, Y., Schurman, M. I., Xu, H., Li, F., Shimada, K., Li, L., Deng, Y., Yai, H., Matsuki, A., Qin, Y., and Zhao, J.: Comparison of Aerosol Hygroscopcity, Volatility, and Chemical Composition between a Suburban Site in the Pearl River Delta Region and a Marine Site in Okinawa, Aerosol and Air Quality Research, 17, 3194–3208, https://doi.org/10.4209/aaqr.2017.01.0020, 2017.

Canagaratna, M. R., Jimenez, J. L., Kroll, J. H., Chen, Q., Kessler, S. H., Massoli, P., Hildebrandt Ruiz, L., Fortner, E., Williams, L. R., Wilson, K. R., Surratt, J. D., Donahue, N. M., Jayne, J. T., and Worsnop, D. R.: Elemental ratio measurements of organic compounds using aerosol mass spectrometry: characterization, improved calibration, and implications, Atmos. Chem. Phys., 15, 253–272, https://doi.org/10.5194/acp-15-253-2015, 2015.

Cerully, K. M., Bougiatioti, A., Hite Jr., J. R., Guo, H., Xu, L., Ng, N. L., Weber, R., and Nenes, A.: On the link between hygroscopicity, volatility, and oxidation state of ambient and water-soluble aerosols in the southeastern United States, Atmos. Chem. Phys., 15, 8679–8694, https://doi.org/10.5194/acp-15-8679-2015, 2015.

Chen, C., Qiu, Y., Xu, W., He, Y., Li, Z., Sun, J., Ma, N., Xu, W., Pan, X., Fu, P., Wang, Z., and Sun, Y.: Primary Emissions and Secondary Aerosol Processing During Wintertime in Rural Area of North China Plain, Journal of Geophysical Research: Atmospheres, 127, e2021JD035430, https://doi.org/10.1029/2021JD035430, 2022.

Chen, J., Budisulistiorini, S. H., Miyakawa, T., Komazaki, Y., and Kuwata, M.: Secondary aerosol formation promotes water uptake by organic-rich wildfire haze particles in equatorial Asia, Atmos. Chem. Phys., 18, 7781–7798, https://doi.org/10.5194/acp-18-7781-2018, 2018.

Cheng, Y. F., Su, H., Rose, D., Gunthe, S. S., Berghof, M., Wehner, B., Achtert, P., Nowak, A., Takegawa, N., Kondo, Y., Shiraiwa, M., Gong, Y. G., Shao, M., Hu, M., Zhu, T., Zhang, Y. H., Carmichael, G. R., Wiedensohler, A., Andreae, M. O., and Pöschl, U.: Size-resolved measurement of the mixing state of soot in the megacity Beijing, China: diurnal cycle, aging and parameterization, Atmos. Chem. Phys., 12, 4477–4491, https://doi.org/10.5194/acp-12-4477-2012, 2012.

Ching, J., Fast, J., West, M., and Riemer, N.: Metrics to quantify the importance of mixing state for CCN activity, Atmos. Chem. Phys., 17, 7445–7458, https://doi.org/10.5194/acp-17-7445-2017, 2017.

Ching, J., Adachi, K., Zaizen, Y., Igarashi, Y., and Kajino, M.: Aerosol mixing state revealed by transmission electron microscopy pertaining to cloud formation and human airway deposition, npj Climate and Atmospheric Science, 2, 22, https://doi.org/10.1038/s41612-019-0081-9, 2019.

Deng, Z. Z., Zhao, C. S., Ma, N., Liu, P. F., Ran, L., Xu, W. Y., Chen, J., Liang, Z., Liang, S., Huang, M. Y., Ma, X. C., Zhang, Q., Quan, J. N., Yan, P., Henning, S., Mildenberger, K., Sommerhage, E., Schäfer, M., Stratmann, F., and Wiedensohler, A.: Size-resolved and bulk activation properties of aerosols in the North China Plain, Atmos. Chem. Phys., 11, 3835–3846, https://doi.org/10.5194/acp-11-3835-2011, 2011.

Deng, Z. Z., Zhao, C. S., Ma, N., Ran, L., Zhou, G. Q., Lu, D. R., and Zhou, X. J.: An examination of parameterizations for the CCN number concentration based on in situ measurements of aerosol activation properties in the North China Plain, Atmos. Chem. Phys., 13, 6227–6237, https://doi.org/10.5194/acp-13-6227-2013, 2013.

Drinovec, L., Močnik, G., Zotter, P., Prévôt, A. S. H., Ruckstuhl, C., Coz, E., Rupakheti, M., Sciare, J., Müller, T., Wiedensohler, A., and Hansen, A. D. A.: The "dual-spot" Aethalometer: an improved measurement of aerosol black carbon with real-time loading compensation, Atmos. Meas. Tech., 8, 1965–1979, https://doi.org/10.5194/amt-8-1965-2015, 2015.

Ervens, B.: Modeling the Processing of Aerosol and Trace Gases in Clouds and Fogs, Chemical Reviews, 115, 4157–4198, https://doi.org/10.1021/cr5005887, 2015.

Farmer, D. K., Cappa, C. D., and Kreidenweis, S. M.: Atmospheric Processes and Their Controlling Influence on Cloud Condensation Nuclei Activity, Chemical Reviews, 115, 4199–4217, https://doi.org/10.1021/cr5006292, 2015.

Fierce, L., Riemer, N., and Bond, T. C.: Toward Reduced Representation of Mixing State for Simulating Aerosol Effects on Climate, Bulletin of the American Meteorological Society, 98, 971–980, https://doi.org/10.1175/BAMS-D-16-0028.1, 2017.

Fu, Y., Peng, X., Sun, W., Hu, X., Wang, D., Yang, Y., Guo, Z., Wang, Y., Zhang, G., Zhu, J., Ou, J., Shi, Z., Wang, X., and Bi, X.: Impact of Cloud Process in the Mixing State and Microphysical Properties of Soot Particles: Implications in Light Absorption Enhancement, Journal of Geophysical Research: Atmospheres, n/a, e2022JD037169, https://doi.org/10.1029/2022JD037169, 2022.

Gysel, M., Laborde, M., Olfert, J. S., Subramanian, R., and Gröhn, A. J.: Effective density of Aquadag and fullerene soot black carbon reference materials used for SP2 calibration, Atmos. Meas. Tech., 4, 2851–2858, https://doi.org/10.5194/amt-4-2851-2011, 2011.

Herich, H., Kammermann, L., Gysel, M., Weingartner, E., Baltensperger, U., Lohmann, U., and Cziczo, D. J.: In situ determination of atmospheric aerosol composition as a function of hygroscopic growth, Journal of Geophysical Research: Atmospheres, 113, https://doi.org/10.1029/2008JD009954, 2008.

Herich, H., Kammermann, L., Friedman, B., Gross, D. S., Weingartner, E., Lohmann, U., Spichtinger, P., Gysel, M., Baltensperger, U., and Cziczo, D. J.: Subarctic atmospheric aerosol composition: 2. Hygroscopic growth properties, Journal of Geophysical Research: Atmospheres, 114, https://doi.org/10.1029/2008JD011574, 2009.

Hong, J., Äijälä, M., Häme, S. A. K., Hao, L., Duplissy, J., Heikkinen, L. M., Nie, W., Mikkilä, J., Kulmala, M., Prisle, N. L., Virtanen, A., Ehn, M., Paasonen, P., Worsnop, D. R., Riipinen, I., Petäjä, T., and Kerminen, V.-M.: Estimates of the organic aerosol volatility in a boreal forest using two independent methods, Atmos. Chem. Phys., 17, 4387–4399, https://doi.org/10.5194/acp-17-4387-2017, 2017.

Jayne, J. T., Leard, D. C., Zhang, X., Davidovits, P., Smith, K. A., Kolb, C. E., and Worsnop, D. R.: Development of an Aerosol Mass Spectrometer for Size and Composition Analysis of Submicron Particles, Aerosol Science and Technology, 33, 49–70, https://doi.org/10.1080/027868200410840, 2000.

Jiang, X., Tao, J., Kuang, Y., Hong, J., and Ma, N.: Mathematical derivation and physical interpretation of particle size-resolved activation ratio based on particle hygroscopicity distribution: Application on global characterization of CCN activity, Atmospheric Environment, 246, 118137, https://doi.org/10.1016/j.atmosenv.2020.118137, 2021.

Jurányi, Z., Tritscher, T., Gysel, M., Laborde, M., Gomes, L., Roberts, G., Baltensperger, U., and Weingartner, E.: Hygroscopic mixing state of urban aerosol derived from size-resolved cloud condensation nuclei measurements during the MEGAPOLI campaign in Paris, Atmos. Chem. Phys., 13, 6431–6446, https://doi.org/10.5194/acp-13-6431-2013, 2013.

Kawana, K., Nakayama, T., and Mochida, M.: Hygroscopicity and CCN activity of atmospheric aerosol particles and their relation to organics: Characteristics of urban aerosols in Nagoya, Japan, Journal of Geophysical Research: Atmospheres, 121, 4100–4121, https://doi.org/10.1002/2015jd023213, 2016.

Kim, N., Yum, S. S., Park, M., Park, J. S., Shin, H. J., and Ahn, J. Y.: Hygroscopicity of urban aerosols and its link to size-resolved chemical composition during spring and summer in Seoul, Korea, Atmos. Chem. Phys., 20, 11245–11262, https://doi.org/10.5194/acp-20-11245-2020, 2020.

Kuang, Y., Zhao, C. S., Tao, J. C., and Ma, N.: Diurnal variations of aerosol optical properties in the North China Plain and their influences on the estimates of direct aerosol radiative effect, Atmos. Chem. Phys., 15, 5761–5772, https://doi.org/10.5194/acp-15-5761-2015, 2015.

Kuang, Y., He, Y., Xu, W., Yuan, B., Zhang, G., Ma, Z., Wu, C., Wang, C., Wang, S., Zhang, S., Tao, J., Ma, N., Su, H., Cheng, Y., Shao, M., and Sun, Y.: Photochemical Aqueous-Phase Reactions

Induce Rapid Daytime Formation of Oxygenated Organic Aerosol on the North China Plain, Environmental Science & Technology, 54, 3849–3860, https://doi.org/10.1021/acs.est.9b06836, 2020.

Kuang, Y., Huang, S., Xue, B., Luo, B., Song, Q., Chen, W., Hu, W., Li, W., Zhao, P., Cai, M., Peng, Y., Qi, J., Li, T., Wang, S., Chen, D., Yue, D., Yuan, B., and Shao, M.: Contrasting effects of secondary organic aerosol formations on organic aerosol hygroscopicity, Atmos. Chem. Phys., 21, 10375–10391, https://doi.org/10.5194/acp-21-10375-2021, 2021.

Kuwata, M. and Kondo, Y.: Dependence of size-resolved CCN spectra on the mixing state of nonvolatile cores observed in Tokyo, Journal of Geophysical Research: Atmospheres, 113, https://doi.org/10.1029/2007JD009761, 2008.

Kuwata, M., Kondo, Y., Mochida, M., Takegawa, N., and Kawamura, K.: Dependence of CCN activity of less volatile particles on the amount of coating observed in Tokyo, Journal of Geophysical Research: Atmospheres, 112, https://doi.org/10.1029/2006JD007758, 2007.

Lack, D. A., Langridge, J. M., Bahreini, R., Cappa, C. D., Middlebrook, A. M., and Schwarz, J. P.: Brown carbon and internal mixing in biomass burning particles, Proceedings of the National Academy of Sciences, 109, 14802–14807, https://doi.org/10.1073/pnas.1206575109, 2012.

Lance, S., Nenes, A., Medina, J., and Smith, J. N.: Mapping the operation of the DMT continuous flow CCN counter, Aerosol science and technology, 40, 242–254, 2006.

Lance, S., Raatikainen, T., Onasch, T. B., Worsnop, D. R., Yu, X. Y., Alexander, M. L., Stolzenburg, M. R., McMurry, P. H., Smith, J. N., and Nenes, A.: Aerosol mixing state, hygroscopic growth and cloud activation efficiency during MIRAGE 2006, Atmos. Chem. Phys., 13, 5049–5062, https://doi.org/10.5194/acp-13-5049-2013, 2013.

Lata, N. N., Zhang, B., Schum, S., Mazzoleni, L., Brimberry, R., Marcus, M. A., Cantrell, W. H., Fialho, P., Mazzoleni, C., and China, S.: Aerosol Composition, Mixing State, and Phase State of Free Tropospheric Particles and Their Role in Ice Cloud Formation, ACS Earth Space Chem., 5, 3499–3510, https://doi.org/10.1021/acsearthspacechem.1c00315, 2021.

Lee, A. K. Y., Rivellini, L.-H., Chen, C.-L., Liu, J., Price, D. J., Betha, R., Russell, L. M., Zhang, X., and Cappa, C. D.: Influences of Primary Emission and Secondary Coating Formation on the Particle Diversity and Mixing State of Black Carbon Particles, Environ. Sci. Technol., 53, 9429–9438, https://doi.org/10.1021/acs.est.9b03064, 2019.

Li, G., Su, H., Ma, N., Tao, J., Kuang, Y., Wang, Q., Hong, J., Zhang, Y., Kuhn, U., and Zhang, S.: Multiphase chemistry experiment in Fogs and Aerosols in the North China Plain (McFAN): integrated analysis and intensive winter campaign 2018, Faraday Discussions, 2021.

Liu, D., Joshi, R., Wang, J., Yu, C., Allan, J. D., Coe, H., Flynn, M. J., Xie, C., Lee, J., Squires, F., Kotthaus, S., Grimmond, S., Ge, X., Sun, Y., and Fu, P.: Contrasting physical properties of black carbon in urban Beijing between winter and summer, Atmos. Chem. Phys., 19, 6749–6769, https://doi.org/10.5194/acp-19-6749-2019, 2019.

Liu, D., Li, S., Hu, D., Kong, S., Cheng, Y., Wu, Y., Ding, S., Hu, K., Zheng, S., Yan, Q., Zheng, H., Zhao, D., Tian, P., Ye, J., Huang, M., and Ding, D.: Evolution of Aerosol Optical Properties from Wood Smoke in Real Atmosphere Influenced by Burning Phase and Solar Radiation, Environ. Sci. Technol., 55, 5677–5688, https://doi.org/10.1021/acs.est.0c07569, 2021.

Liu, K., Zhang, C., Cheng, Y., Liu, C., Zhang, H., Zhang, G., Sun, X., and Mu, Y.: Serious BTEX pollution in rural area of the North China Plain during winter season, Journal of Environmental Sciences, 30, 186–190, https://doi.org/10.1016/j.jes.2014.05.056, 2015.

Liu, P. F., Zhao, C. S., Göbel, T., Hallbauer, E., Nowak, A., Ran, L., Xu, W. Y., Deng, Z. Z., Ma, N., and Mildenberger, K.: Hygroscopic properties of aerosol particles at high relative humidity and their diurnal variations in the North China Plain, Atmos. Chem. Phys, 11, 3479–3494, 2011.

Luo, B., Kuang, Y., Huang, S., Song, Q., Hu, W., Li, W., Peng, Y., Chen, D., Yue, D., Yuan, B., and Shao, M.: Parameterizations of size distribution and refractive index of biomass burning organic aerosol with black carbon content, Atmos. Chem. Phys., 22, 12401–12415, https://doi.org/10.5194/acp-22-12401-2022, 2022.

Ma, N., Zhao, C. S., Müller, T., Cheng, Y. F., Liu, P. F., Deng, Z. Z., Xu, W. Y., Ran, L., Nekat, B., van Pinxteren, D., Gnauk, T., Müller, K., Herrmann, H., Yan, P., Zhou, X. J., and Wiedensohler, A.: A new method to determine the mixing state of light absorbing carbonaceous using the measured aerosol optical properties and number size distributions, Atmos. Chem. Phys., 12, 2381–2397, https://doi.org/10.5194/acp-12-2381-2012, 2012.

Ma, N., Zhao, C., Tao, J., Wu, Z., Kecorius, S., Wang, Z., Größ, J., Liu, H., Bian, Y., Kuang, Y., Teich, M., Spindler, G., Müller, K., van Pinxteren, D., Herrmann, H., Hu, M., and Wiedensohler, A.: Variation of CCN activity during new particle formation events in the North China Plain, Atmos. Chem. Phys., 16, 8593–8607, https://doi.org/10.5194/acp-16-8593-2016, 2016.

Matsui, H., Hamilton, D. S., and Mahowald, N. M.: Black carbon radiative effects highly sensitive to emitted particle size when resolving mixing-state diversity, Nature Communications, 9, 3446, https://doi.org/10.1038/s41467-018-05635-1, 2018.

Mei, F., Hayes, P. L., Ortega, A., Taylor, J. W., Allan, J. D., Gilman, J., Kuster, W., de Gouw, J., Jimenez, J. L., and Wang, J.: Droplet activation properties of organic aerosols observed at an urban site during CalNex-LA, Journal of Geophysical Research-Atmospheres, 118, 2903–2917, https://doi.org/10.1002/jgrd.50285, 2013.

Metcalf, A. R., Craven, J. S., Ensberg, J. J., Brioude, J., Angevine, W., Sorooshian, A., Duong, H. T., Jonsson, H. H., Flagan, R. C., and Seinfeld, J. H.: Black carbon aerosol over the Los Angeles Basin during CalNex, Journal of Geophysical Research: Atmospheres, 117, https://doi.org/10.1029/2011JD017255, 2012.

Middlebrook, A. M., Bahreini, R., Jimenez, J. L., and Canagaratna, M. R.: Evaluation of Composition-Dependent Collection Efficiencies for the Aerodyne Aerosol Mass Spectrometer using Field Data, Aerosol Science and Technology, 46, 258–271, https://doi.org/10.1080/02786826.2011.620041, 2012.

Moffet, R. C., O'Brien, R. E., Alpert, P. A., Kelly, S. T., Pham, D. Q., Gilles, M. K., Knopf, D. A., and Laskin, A.: Morphology and mixing of black carbon particles collected in central California during the CARES field study, Atmos. Chem. Phys., 16, 14515–14525, https://doi.org/10.5194/acp-16-14515-2016, 2016.

Mohr, C., Huffman, J. A., Cubison, M. J., Aiken, A. C., Docherty, K. S., Kimmel, J. R., Ulbrich, I. M., Hannigan, M., and Jimenez, J. L.: Characterization of Primary Organic Aerosol Emissions from

Meat Cooking, Trash Burning, and Motor Vehicles with High-Resolution Aerosol Mass Spectrometry and Comparison with Ambient and Chamber Observations, Environ. Sci. Technol., 43, 2443–2449, https://doi.org/10.1021/es8011518, 2009.

Moteki, N. and Kondo, Y.: Effects of Mixing State on Black Carbon Measurements by Laser-Induced Incandescence, Aerosol Science and Technology, 41, 398–417, https://doi.org/10.1080/02786820701199728, 2007.

Nordmann, S., Cheng, Y. F., Carmichael, G. R., Yu, M., Denier van der Gon, H. A. C., Zhang, Q., Saide, P. E., Pöschl, U., Su, H., Birmili, W., and Wiedensohler, A.: Atmospheric black carbon and warming effects influenced by the source and absorption enhancement in central Europe, Atmos. Chem. Phys., 14, 12683–12699, https://doi.org/10.5194/acp-14-12683-2014, 2014.

Paatero, P. and Tapper, U.: Positive matrix factorization: A non-negative factor model with optimal utilization of error estimates of data values, Environmetrics, 5, 111–126, https://doi.org/10.1002/env.3170050203, 1994.

Peng, J., Hu, M., Guo, S., Du, Z., Zheng, J., Shang, D., Levy Zamora, M., Zeng, L., Shao, M., Wu, Y.-S., Zheng, J., Wang, Y., Glen, C. R., Collins, D. R., Molina, M. J., and Zhang, R.: Markedly enhanced absorption and direct radiative forcing of black carbon under polluted urban environments, Proceedings of the National Academy of Sciences, 113, 4266–4271, https://doi.org/10.1073/pnas.1602310113, 2016.

Philippin, S., Wiedensohler, A., and Stratmann, F.: Measurements of non-volatile fractions of pollution aerosols with an eight-tube volatility tandem differential mobility analyzer (VTDMA-8), Journal of Aerosol Science, 35, 185–203, https://doi.org/10.1016/j.jaerosci.2003.07.004, 2004.

Ren, J., Zhang, F., Wang, Y., Collins, D., Fan, X., Jin, X., Xu, W., Sun, Y., Cribb, M., and Li, Z.: Using different assumptions of aerosol mixing state and chemical composition to predict CCN concentrations based on field measurements in urban Beijing, Atmospheric Chemistry and Physics, 18, 6907–6921, https://doi.org/10.5194/acp-18-6907-2018, 2018.

Riemer, N., Ault, A. P., West, M., Craig, R. L., and Curtis, J. H.: Aerosol Mixing State: Measurements, Modeling, and Impacts, Reviews of Geophysics, 57, 187–249, https://doi.org/10.1029/2018RG000615, 2019.

Roberts, G. C. and Nenes, A.: A continuous-flow streamwise thermal-gradient CCN chamber for atmospheric measurements, Aerosol science and technology, 39, 206–221, 2005.

Rose, D., Gunthe, S. S., Mikhailov, E., Frank, G. P., Dusek, U., Andreae, M. O., and Pöschl, U.: Calibration and measurement uncertainties of a continuous-flow cloud condensation nuclei counter (DMT-CCNC): CCN activation of ammonium sulfate and sodium chloride aerosol particles in theory and experiment, Atmos. Chem. Phys., 8, 1153–1179, 2008.

Rose, D., Nowak, A., Achtert, P., Wiedensohler, A., Hu, M., Shao, M., Zhang, Y., Andreae, M. O., and Poschl, U.: Cloud condensation nuclei in polluted air and biomass burning smoke near the mega-city Guangzhou, China - Part 1: Size-resolved measurements and implications for the modeling of aerosol particle hygroscopicity and CCN activity, Atmos. Chem. Phys., 10, 3365–3383, 2010.

Rose, D., Gunthe, S. S., Su, H., Garland, R. M., Yang, H., Berghof, M., Cheng, Y. F., Wehner, B., Achtert, P., Nowak, A., Wiedensohler, A., Takegawa, N., Kondo, Y., Hu, M., Zhang, Y., Andreae,

893 M. O., and Poschl, U.: Cloud condensation nuclei in polluted air and biomass burning smoke near the
894 mega-city Guangzhou, China -Part 2: Size-resolved aerosol chemical composition, diurnal cycles, and
895 externally mixed weakly CCN-active soot particles, Atmos. Chem. Phys., 11, 2817–2836,
896 https://doi.org/10.5194/acp-11-2817-2011, 2011.

897 Saha, P. K., Khlystov, A., and Grieshop, A. P.: Downwind evolution of the volatility and mixing
898 state of near-road aerosols near a US interstate highway, Atmos. Chem. Phys., 18, 2139–2154,
899 https://doi.org/10.5194/acp-18-2139-2018, 2018.

900 Sedlacek, A. J., Lewis, E. R., Kleinman, L., Xu, J., and Zhang, Q.: Determination of and evidence
901 for non-core-shell structure of particles containing black carbon using the Single-Particle Soot
902 Photometer (SP2), Geophysical Research Letters, 39, L06802, https://doi.org/10.1029/2012GL050905,
903 2012.

904 Shi, J., Hong, J., Ma, N., Luo, Q., He, Y., Xu, H., Tan, H., Wang, Q., Tao, J., Zhou, Y., Han, S.,
905 Peng, L., Xie, L., Zhou, G., Xu, W., Sun, Y., Cheng, Y., and Su, H.: Measurement report: On the
906 difference in aerosol hygroscopicity between high and low relative humidity conditions in the North
907 China Plain, Atmos. Chem. Phys., 22, 4599–4613, https://doi.org/10.5194/acp-22-4599-2022, 2022.

908 Stevens, R., Ryjkov, A., Majdzadeh, M., and Dastoor, A.: An improved representation of aerosol
909 mixing state for air quality–weather interactions, Atmos. Chem. Phys., 22, 13527–13549,
910 https://doi.org/10.5194/acp-22-13527-2022, 2022.

911 Stolzenburg, M. R. and McMurry, P. H.: Equations governing single and tandem DMA
912 configurations and a new lognormal approximation to the transfer function, Aerosol Science and
913 Technology, 42, 421–432, 2008.

914 Su, H., Rose, D., Cheng, Y. F., Gunthe, S. S., Massling, A., Stock, M., Wiedensohler, A., Andreae,
915 M. O., and Poschl, U.: Hygroscopicity distribution concept for measurement data analysis and
916 modeling of aerosol particle mixing state with regard to hygroscopic growth and CCN activation,
917 Atmos. Chem. Phys., 10, 7489–7503, https://doi.org/10.5194/acp-10-7489-2010, 2010.

918 Subramanian, R., Kok, G. L., Baumgardner, D., Clarke, A., Shinozuka, Y., Campos, T. L., Heizer,
919 C. G., Stephens, B. B., de Foy, B., Voss, P. B., and Zaveri, R. A.: Black carbon over Mexico: the effect
920 of atmospheric transport on mixing state, mass absorption cross-section, and BC/CO ratios, Atmos.
921 Chem. Phys., 10, 219–237, https://doi.org/10.5194/acp-10-219-2010, 2010.

922 Tan, H., Xu, H., Wan, Q., Li, F., Deng, X., Chan, P. W., Xia, D., and Yin, Y.: Design and
923 Application of an Unattended Multifunctional H-TDMA System, Journal of Atmospheric and Oceanic
924 Technology, 30, 1136–1148, https://doi.org/10.1175/JTECH-D-12-00129.1, 2013.

925 Tao, J., Zhao, C., Nan, M., and Ye, K.: Consistency and applicability of parameterization schemes
926 for the size-resolved aerosol activation ratio based on field measurements in the North China Plain,
927 Atmospheric Environment, 173, 316–324, 2018.

928 Tao, J., Kuang, Y., Ma, N., Zheng, Y., Wiedensohler, A., and Zhao, C.: An improved
929 parameterization scheme for size-resolved particle activation ratio and its application on comparison
930 study of particle hygroscopicity measurements between HTDMA and DMA-CCNC, Atmospheric
931 Environment, 226, 117403, https://doi.org/10.1016/j.atmosenv.2020.117403, 2020.

Tao, J., Kuang, Y., Ma, N., Hong, J., Sun, Y., Xu, W., Zhang, Y., He, Y., Luo, Q., Xie, L., Su, H., and Cheng, Y.: Secondary aerosol formation alters CCN activity in the North China Plain, Atmos. Chem. Phys., 21, 7409–7427, https://doi.org/10.5194/acp-21-7409-2021, 2021.

Tao, M., Chen, L., Su, L., and Tao, J.: Satellite observation of regional haze pollution over the North China Plain, Journal of Geophysical Research: Atmospheres, 117, https://doi.org/10.1029/2012JD017915, 2012.

Thalman, R., de Sa, S. S., Palm, B. B., Barbosa, H. M. J., Poehlker, M. L., Alexander, M. L., Brito, J., Carbone, S., Castillo, P., Day, D. A., Kuang, C., Manzi, A., Ng, N. L., Sedlacek, A. J., Souza, R., Springston, S., Watson, T., Poehlker, C., Poeschl, U., Andreae, M. O., Artaxo, P., Jimenez, J. L., Martin, S. T., and Wang, J.: CCN activity and organic hygroscopicity of aerosols downwind of an urban region in central Amazonia: seasonal and diel variations and impact of anthropogenic emissions, Atmospheric Chemistry and Physics, 17, 11779–11801, https://doi.org/10.5194/acp-17-11779-2017, 2017.

Ting, Y., Mitchell, E. J. S., Allan, J. D., Liu, D., Spracklen, D. V., Williams, A., Jones, J. M., Lea-Langton, A. R., McFiggans, G., and Coe, H.: Mixing State of Carbonaceous Aerosols of Primary Emissions from "Improved" African Cookstoves, Environ. Sci. Technol., 52, 10134–10143, https://doi.org/10.1021/acs.est.8b00456, 2018.

Tomlin, J. M., Jankowski, K. A., Veghte, D. P., China, S., Wang, P., Fraund, M., Weis, J., Zheng, G., Wang, Y., Rivera-Adorno, F., Raveh-Rubin, S., Knopf, D. A., Wang, J., Gilles, M. K., Moffet, R. C., and Laskin, A.: Impact of dry intrusion events on the composition and mixing state of particles during the winter Aerosol and Cloud Experiment in the Eastern North Atlantic (ACE-ENA), Atmos. Chem. Phys., 21, 18123–18146, https://doi.org/10.5194/acp-21-18123-2021, 2021.

Ulbrich, I. M., Canagaratna, M. R., Zhang, Q., Worsnop, D. R., and Jimenez, J. L.: Interpretation of organic components from Positive Matrix Factorization of aerosol mass spectrometric data, Atmos. Chem. Phys., 9, 2891–2918, https://doi.org/10.5194/acp-9-2891-2009, 2009.

Wang, X., Ye, X., Chen, J., Wang, X., Yang, X., Fu, T.-M., Zhu, L., and Liu, C.: Direct links between hygroscopicity and mixing state of ambient aerosols: estimating particle hygroscopicity from their single-particle mass spectra, Atmos. Chem. Phys., 20, 6273–6290, https://doi.org/10.5194/acp-20-6273-2020, 2020.

Wang, Y., Wang, X., Kondo, Y., Kajino, M., Munger, J. W., and Hao, J.: Black carbon and its correlation with trace gases at a rural site in Beijing: Top-down constraints from ambient measurements on bottom-up emissions, Journal of Geophysical Research: Atmospheres, 116, https://doi.org/10.1029/2011JD016575, 2011.

Wang, Y., Zhang, F., Li, Z., Tan, H., Xu, H., Ren, J., Zhao, J., Du, W., and Sun, Y.: Enhanced hydrophobicity and volatility of submicron aerosols under severe emission control conditions in Beijing, Atmos. Chem. Phys., 17, 5239–5251, https://doi.org/10.5194/acp-17-5239-2017, 2017.

Wang, Y., Hu, R., Wang, Q., Li, Z., Cribb, M., Sun, Y., Song, X., Shang, Y., Wu, Y., Huang, X., and Wang, Y.: Different effects of anthropogenic emissions and aging processes on the mixing state of soot particles in the nucleation and accumulation modes, Atmos. Chem. Phys., 22, 14133–14146, https://doi.org/10.5194/acp-22-14133-2022, 2022.

Wehner, B., Berghof, M., Cheng, Y. F., Achtert, P., Birmili, W., Nowak, A., Wiedensohler, A., Garland, R. M., Pöschl, U., Hu, M., and Zhu, T.: Mixing state of nonvolatile aerosol particle fractions and comparison with light absorption in the polluted Beijing region, Journal of Geophysical Research: Atmospheres, 114, https://doi.org/10.1029/2008JD010923, 2009.

Wu, Y., Wang, X., Tao, J., Huang, R., Tian, P., Cao, J., Zhang, L., Ho, K.-F., Han, Z., and Zhang, R.: Size distribution and source of black carbon aerosol in urban Beijing during winter haze episodes, Atmos. Chem. Phys., 17, 7965–7975, https://doi.org/10.5194/acp-17-7965-2017, 2017.

Xu, W., Sun, Y., Wang, Q., Zhao, J., Wang, J., Ge, X., Xie, C., Zhou, W., Du, W., Li, J., Fu, P., Wang, Z., Worsnop, D. R., and Coe, H.: Changes in Aerosol Chemistry From 2014 to 2016 in Winter in Beijing: Insights From High-Resolution Aerosol Mass Spectrometry, Journal of Geophysical Research: Atmospheres, 124, 1132–1147, https://doi.org/10.1029/2018JD029245, 2019.

Xu, W. Y., Zhao, C. S., Ran, L., Deng, Z. Z., Liu, P. F., Ma, N., Lin, W. L., Xu, X. B., Yan, P., He, X., Yu, J., Liang, W. D., and Chen, L. L.: Characteristics of pollutants and their correlation to meteorological conditions at a suburban site in the North China Plain, Atmos. Chem. Phys., 11, 4353–4369, https://doi.org/10.5194/acp-11-4353-2011, 2011.

Yang, Z., Ma, N., Wang, Q., Li, G., Pan, X., Dong, W., Zhu, S., Zhang, S., Gao, W., He, Y., Xie, L., Zhang, Y., Kuhn, U., Xu, W., Kuang, Y., Tao, J., Hong, J., Zhou, G., Sun, Y., Su, H., and Cheng, Y.: Characteristics and source apportionment of black carbon aerosol in the North China Plain, Atmospheric Research, 276, 106246, https://doi.org/10.1016/j.atmosres.2022.106246, 2022.

Zhang, F., Li, Y., Li, Z., Sun, L., Li, R., Zhao, C., Wang, P., Sun, Y., Liu, X., Li, J., Li, P., Ren, G., and Fan, T.: Aerosol hygroscopicity and cloud condensation nuclei activity during the AC3Exp campaign: implications for cloud condensation nuclei parameterization, Atmos. Chem. Phys., 14, 13423–13437, https://doi.org/10.5194/acp-14-13423-2014, 2014.

Zhang, S., Shen, X., Sun, J., Zhang, Y., Zhang, X., Xia, C., Hu, X., Zhong, J., Wang, J., and Liu, S.: Atmospheric Particle Hygroscopicity and the Influence by Oxidation State of Organic Aerosols in Urban Beijing, Journal of Environmental Sciences, 124, 544–556, https://doi.org/10.1016/j.jes.2021.11.019, 2023.

Zhang, S. L., Ma, N., Kecorius, S., Wang, P. C., Hu, M., Wang, Z. B., Größ, J., Wu, Z. J., and Wiedensohler, A.: Mixing state of atmospheric particles over the North China Plain, Atmospheric Environment, 125, 152–164, 2016.

Zhang, Y., Su, H., Ma, N., Li, G., Kecorius, S., Wang, Z., Hu, M., Zhu, T., He, K., Wiedensohler, A., Zhang, Q., and Cheng, Y.: Sizing of Ambient Particles From a Single-Particle Soot Photometer Measurement to Retrieve Mixing State of Black Carbon at a Regional Site of the North China Plain, Journal of Geophysical Research: Atmospheres, 123, 12,778-12,795, https://doi.org/10.1029/2018JD028810, 2018.

Zhao, G., Tao, J., Kuang, Y., Shen, C., Yu, Y., and Zhao, C.: Role of black carbon mass size distribution in the direct aerosol radiative forcing, Atmos. Chem. Phys., 19, 13175–13188, https://doi.org/10.5194/acp-19-13175-2019, 2019.

Zhao, G., Tan, T., Hu, S., Du, Z., Shang, D., Wu, Z., Guo, S., Zheng, J., Zhu, W., Li, M., Zeng, L., and Hu, M.: Mixing state of black carbon at different atmospheres in north and southwest China, Atmos. Chem. Phys., 22, 10861–10873, https://doi.org/10.5194/acp-22-10861-2022, 2022.

Zheng, H., Kong, S., Wu, F., Cheng, Y., Niu, Z., Zheng, S., Yang, G., Yao, L., Yan, Q., Wu, J., Zheng, M., Chen, N., Xu, K., Yan, Y., Liu, D., Zhao, D., Zhao, T., Bai, Y., Li, S., and Qi, S.: Intra-regional transport of black carbon between the south edge of the North China Plain and central China during winter haze episodes, Atmos. Chem. Phys., 19, 4499–4516, https://doi.org/10.5194/acp-19-4499-2019, 2019.

Zhuang, B. L., Li, S., Wang, T. J., Deng, J. J., Xie, M., Yin, C. Q., and Zhu, J. L.: Direct radiative forcing and climate effects of anthropogenic aerosols with different mixing states over China, Atmospheric Environment, 79, 349–361, https://doi.org/10.1016/j.atmosenv.2013.07.004, 2013.

Table 1. Definitions and descriptions of abbreviations.

Abbreviation	Full name and/or Definition
BBOA	Biomass Burning Organic Aerosol Characterized by obvious m/z 60 (mainly $C_2H_4O_2^+$) and 73 (mainly $C_3H_5O_2^+$), which are two indicators of biomass burning
FFOA	Fossil Fuel Organic Aerosol A mixed factor that comprises traffic emissions and coal combustion, which was characterized by typical hydrocarbon ion series
OOA	Oxygenated Organic Aerosol
OOA1 and OOA2	Two OOA factors resolved from the PMF analysis
SOA	Secondary Organic Aerosol Summation of OOA1 and OOA2
POA	Primary Organic Aerosol Summation of BBOA and FFOA
SIA	Secondary Inorganic Aerosols, including nitrate, sulfate, and ammonium
$PM_{2.5}$	Particulate Matter with an aerodynamic diameter <2.5 μm
PM_1	Particulate Matter with an aerodynamic diameter <1 μm
$NR\text{-}PM_1$	Non-refractory PM_1
MF	Mass Fraction
D_p	Particle diameter after humidification or heating
D_d	Particle diameter under dry conditions without humidification or heating
κ	Hygroscopicity parameter
SS	Supersaturation
SPAR	Size-resolved Particle Activation Ratio

|	Size-dependent CCN activity under a specific SS
MAF	Maximum Activation Fraction
	An asymptote of the measured SPAR curve at large particle sizes and represents the number fraction of CCNs to total particles
D_a	Midpoint activation diameter
	Linked to the hygroscopicity of CCNs
GF	Growth factor
	The ratio between particles with and without humidification and is linked to aerosol hygroscopicity
SF	Shrinkage Factor
	The ratio between particles with and without heating and is linked to aerosol volatility
PDF	Probability Distribution Function
NF_H	Number Fraction of Hydrophilic aerosol whose hygroscopicity parameter is >~0.07
NF_V	Number Fraction of Volatile aerosol whose Shrinkage Factor at 200 °C is <0.85
NF_{noBC}	Number Fraction of black carbon (BC)-free particles
NF_{CBC}	Number Fraction of thickly coated BC particles
R_{exBC}	The number concentration ratio of externally mixed BC particles in total BC-containing particles
	Externally mixed BC particles are defined as identified bare/thinly coated BC-containing particles
NF_A-NF_B (NF$_{noBC}$-NF$_H$, NF$_V$-NF$_H$, NF$_{noBC}$-NF$_V$, NF$_V$-MAF, NF$_{noBC}$-MAF)	The difference between the number fraction of A and B

1022
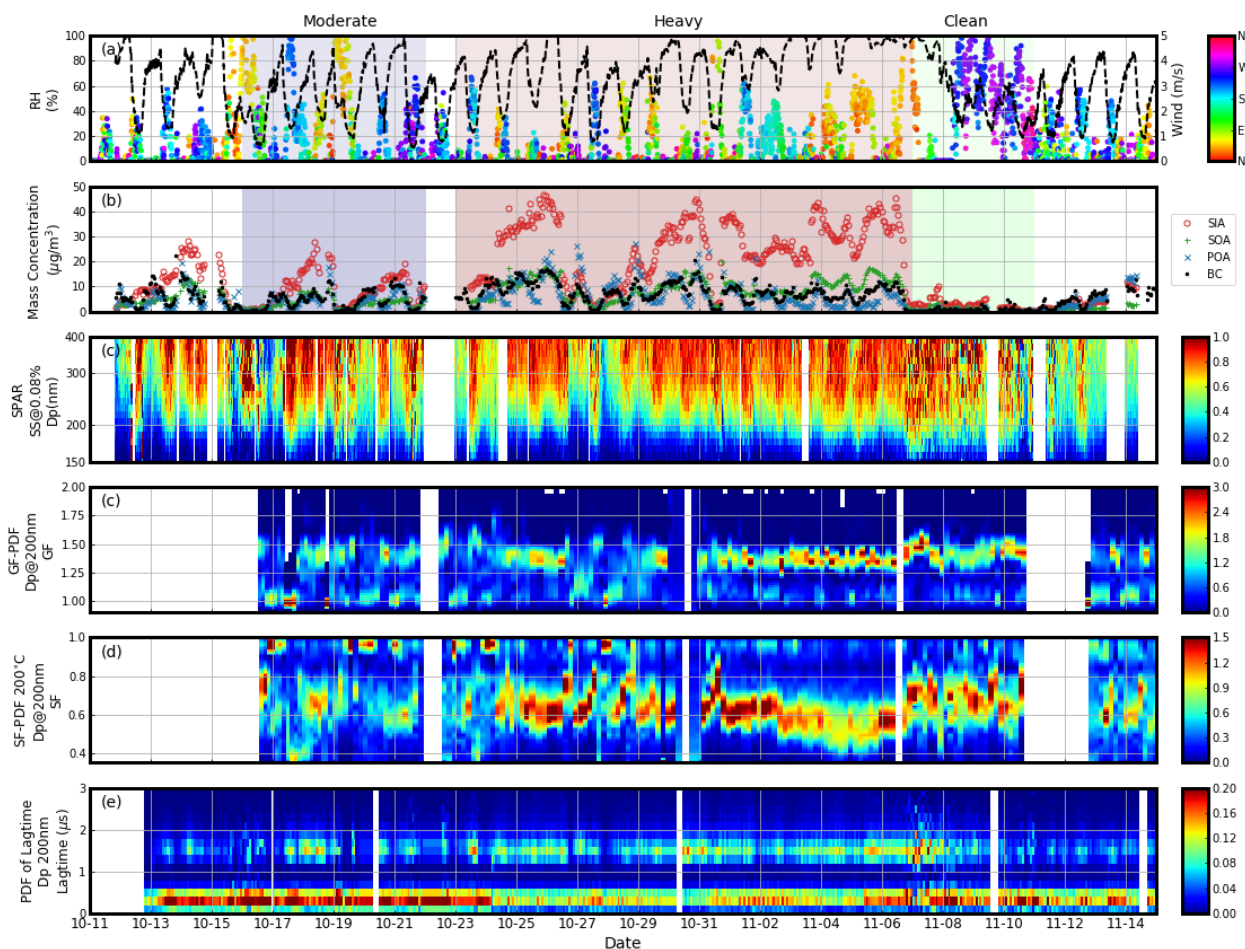
Figure 1. Overview of the measurements during the campaign: **(a)** meteorological parameters: wind speed (dots) and relative humidity (RH) (black line), with colors of dots representing wind direction; **(b)** mass concentrations of aerosol chemical compositions: secondary inorganic aerosols (SIA, red circle), secondary organic aerosols (SOA, green plus), primary organic aerosols (POA, blue x) and black carbon (BC, black dots); **(c)** Size-resolved Particle Activation Ratio (SPAR) under supersaturation (SS) of 0.08% observed by the DMA-CCNC, with warmer colors corresponding to higher values; **(d)** Probability Density Function (PDF) of growth factor (GF-PDF) at 200 nm observed by the HTDMA; **(e)** PDF of shrinkage factor (SF-PDF) at 200 nm and 200 °C observed by the VTDMA; **(f)** PDF of lag time at 200 nm observed by the DMA-SP2. The blue, red, and green shaded periods represent the three periods with moderate pollution, heavy pollution, and clean conditions, respectively.
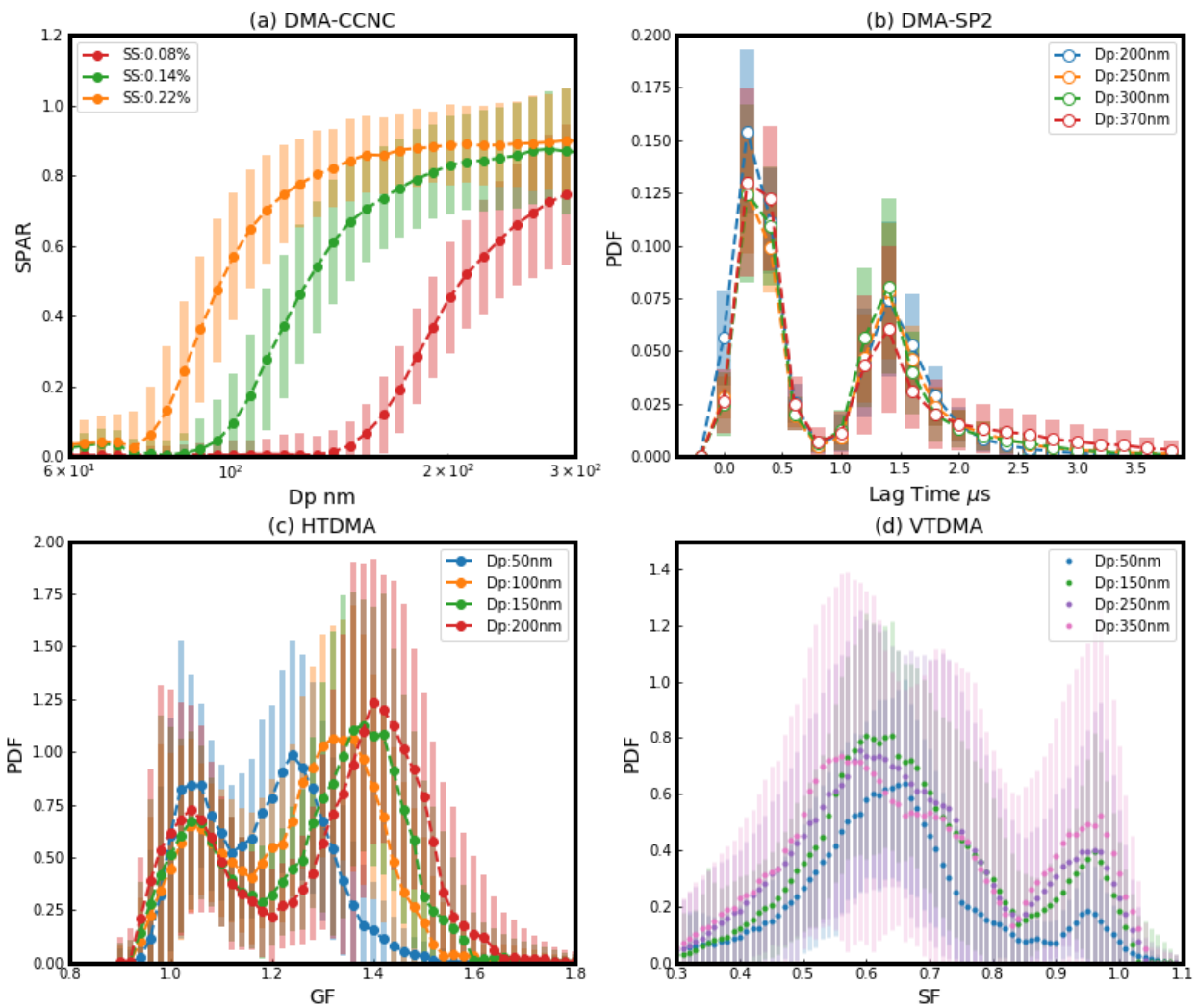
1033

Figure 2. The campaign average of **(a)** Size-resolved Particle Activation Ratio (SPAR) curves measured by DMA-CCNC at the three supersaturations (SSs, represented by different colors and markers), **(b)** Probability Density Function (PDF) of lag time measured by DMA-SP2 at four particle sizes (represented by different colors and markers), **(c)** PDF of growth factor (GF) measured by HTDMA at four particle sizes (represented by different colors and markers), **(d)** PDF of shrinkage factor (SF) measured by VTDMA under the temperature of 200 °C at five particle sizes (represented by different colors and markers). The shaded areas indicate the standard deviations.
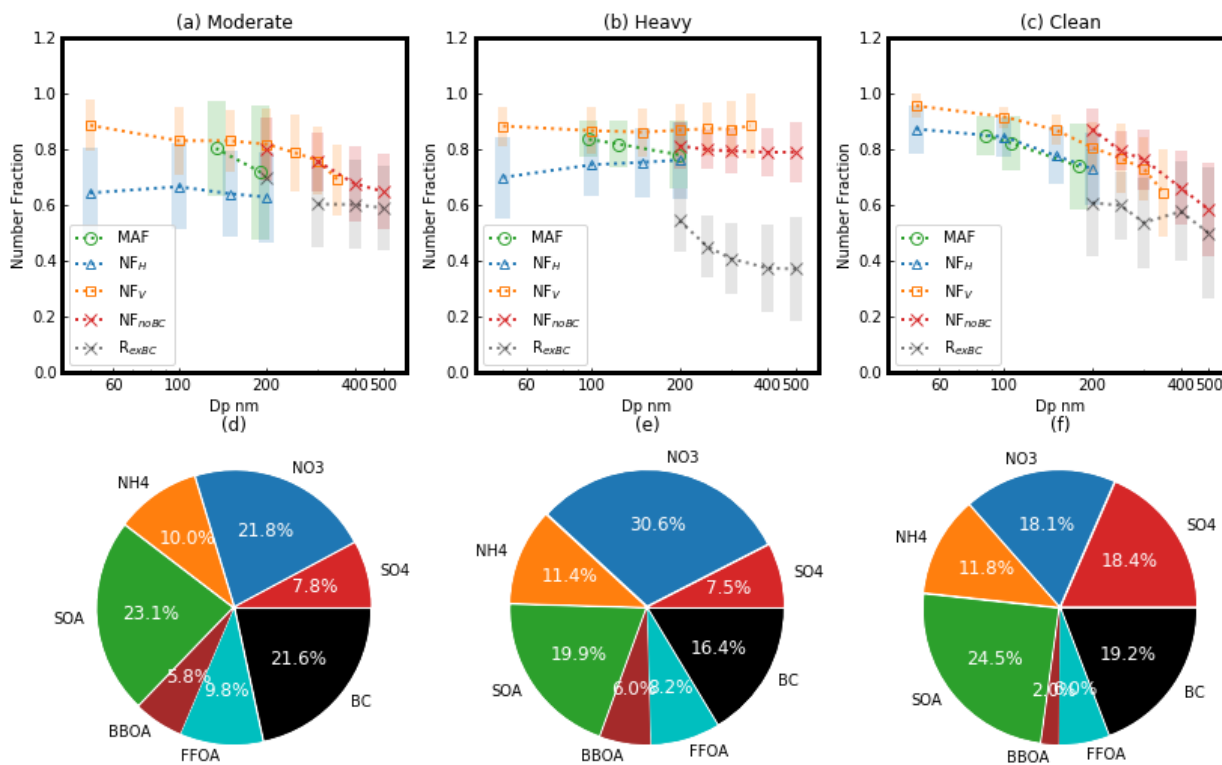
Figure 3. **(a–c)** Size dependence of MAF (green circle), NF_H (blue triangle), NF_V (yellow square), NF_{noBC} (red x), and R_{exBC} (black x) during the three periods. **MAF**: Maximum Activation Fraction, an asymptote of the measured Size-resolved Particle Activation Ratio (SPAR) curve at large particle. **NF_H**: Number Fraction of Hydrophilic aerosol whose hygroscopicity parameter is higher than ~0.07. **NF_V**: Number Fraction of Volatile aerosol whose Shrink Factor at 200 °C is lower than 0.85. **NF_{noBC}**: Number Fraction of black carbon (BC)-free particles. **R_{exBC}**: Number fraction of externally mixed BC particles in total BC-containing particles. **(d–f)** Corresponding mass fractions (MFs) of aerosol chemical compositions (identified by colors) during the three periods, including secondary organic aerosols (SOA), biomass burning organic aerosol (BBOA), fossil fuel organic aerosols (FFOA), and inorganic ions including sulfate (SO_4), nitrate (NO_3), and ammonium (NH_4).
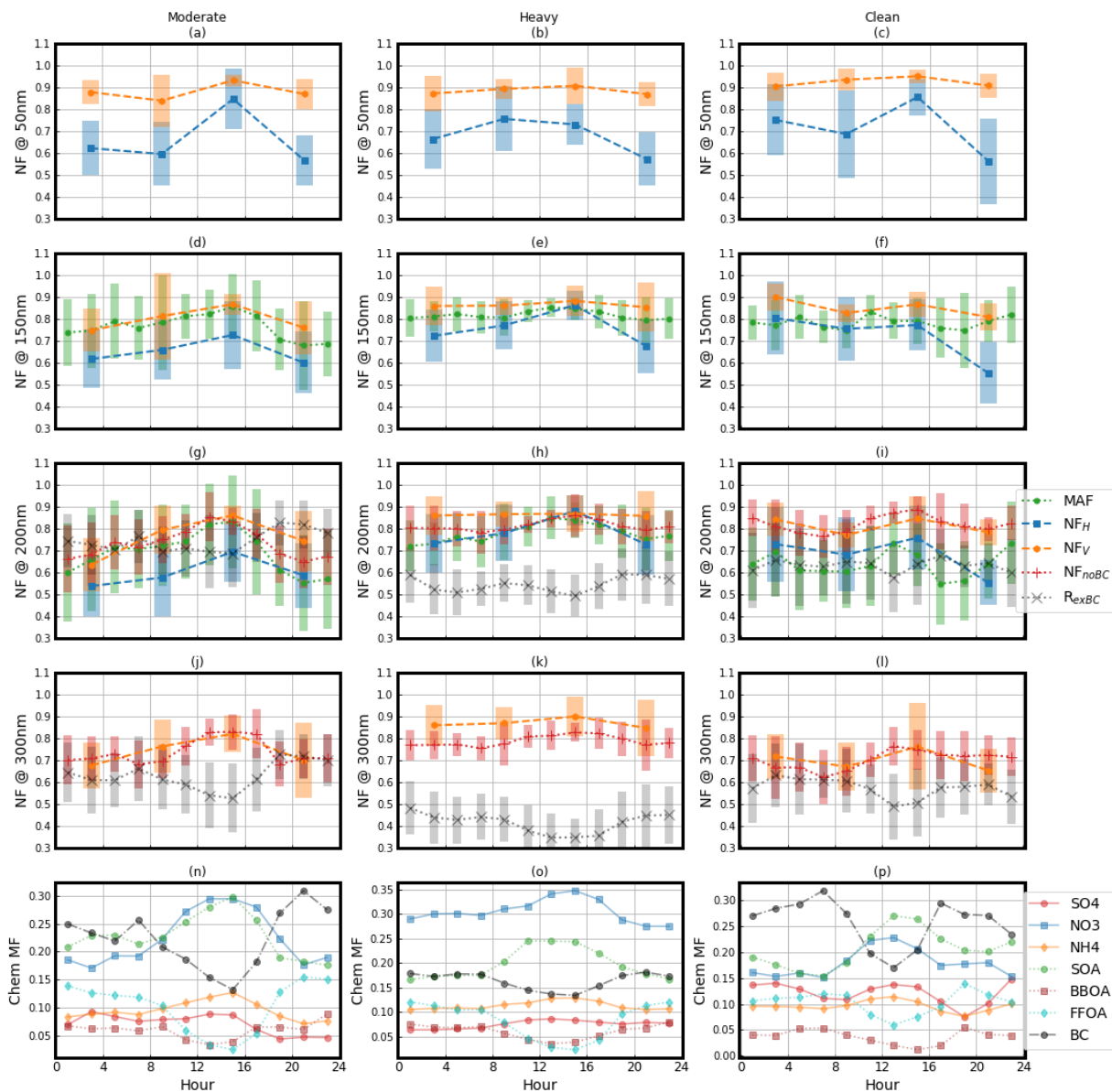
Figure 4. (a–l) Diurnal variations of aerosol mixing state parameters (identified by color and marker) at different particle sizes (50, 150, 200, and 300 nm) during the three periods. The shaded areas indicate the standard deviations. **(m–o)** Diurnal variations of mass fractions (MFs) of aerosol chemical compositions, including secondary organic aerosols (SOA), biomass burning organic aerosol (BBOA), fossil fuel organic aerosols (FFOA), and inorganic ions including sulfate (SO_4), nitrate (NO_3), and ammonium (NH_4) (identified by color and marker) during the three periods.
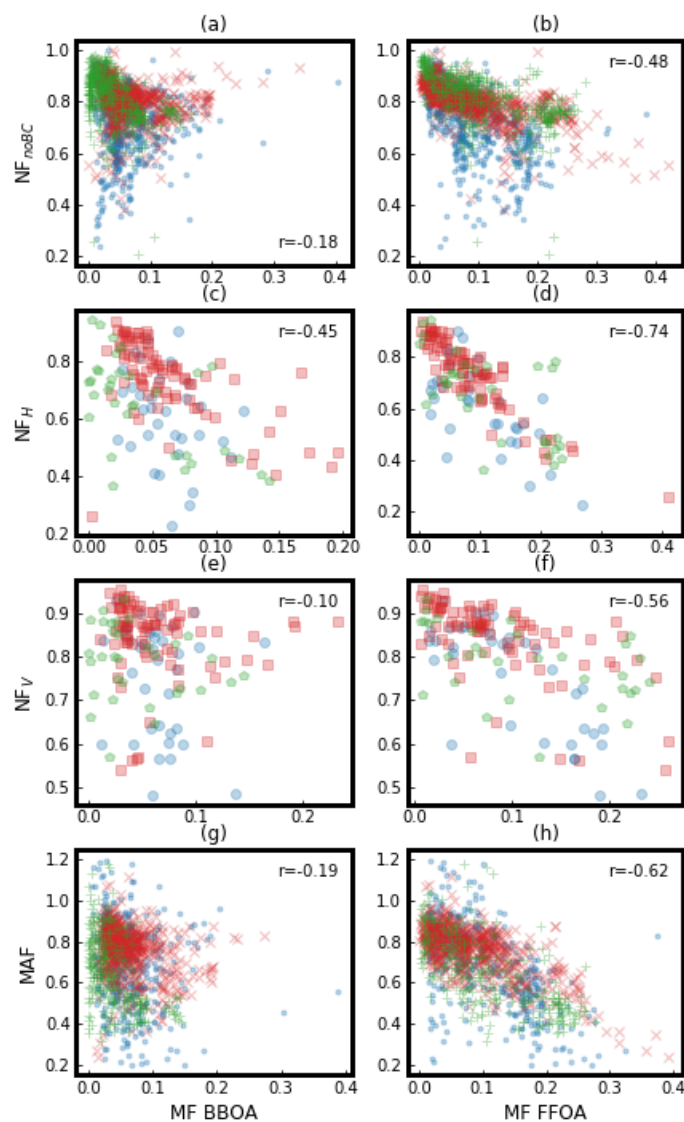
Figure 5. The correlations between aerosol mixing state parameters and mass fractions (MFs) of biomass burning organic aerosol (BBOA) and fossil fuel organic aerosols (FFOA) during different periods (moderately polluted period: blue dot or circle; heavily polluted period: red x or square; clean period: green plus or pentagon), with r representing the correlation coefficient.
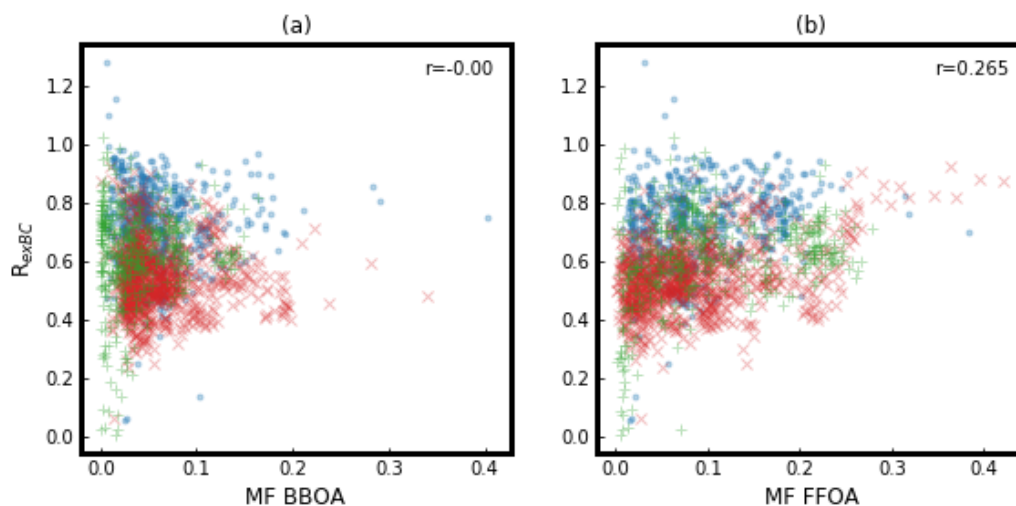
1062
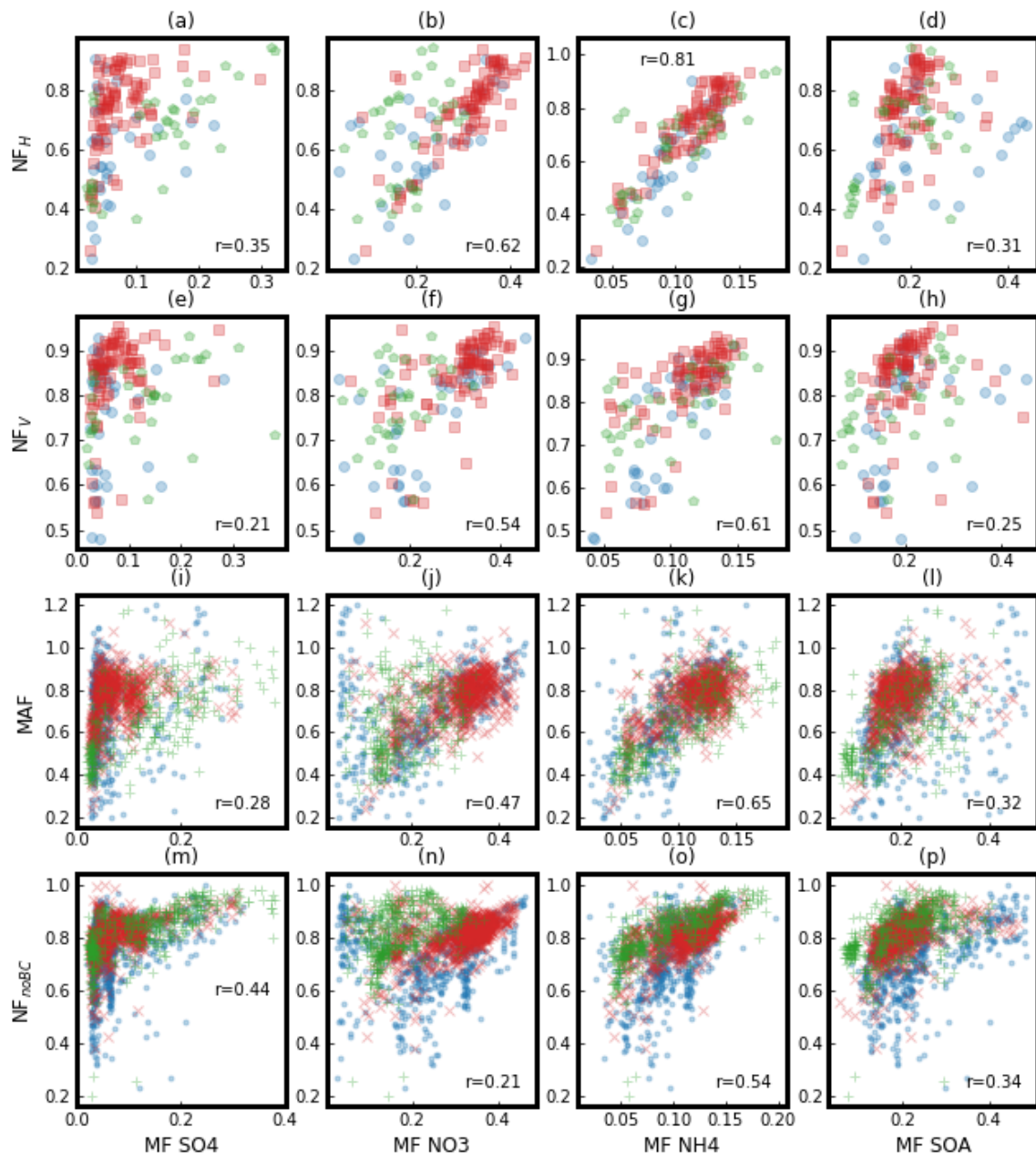
Figure 6. The correlations between the ratio of externally mixed black carbon (BC) in total BC particles (R_{exBC}) and mass fractions (MFs) of biomass-burning organic aerosol (**BBOA**) and fossil fuel organic aerosols (**FFOA**) during different periods (moderately polluted period: blue dot; heavily polluted period: red x; clean period: green plus), with r representing correlation coefficient.
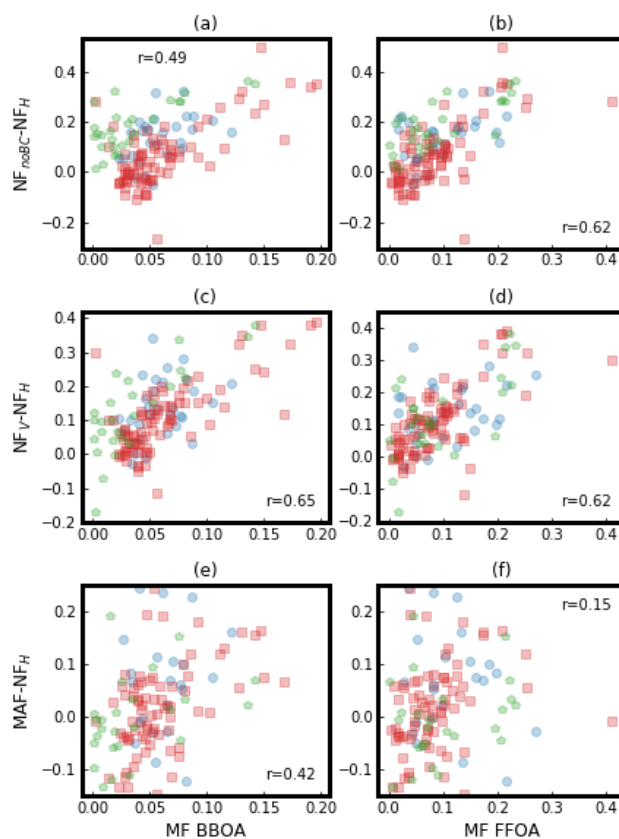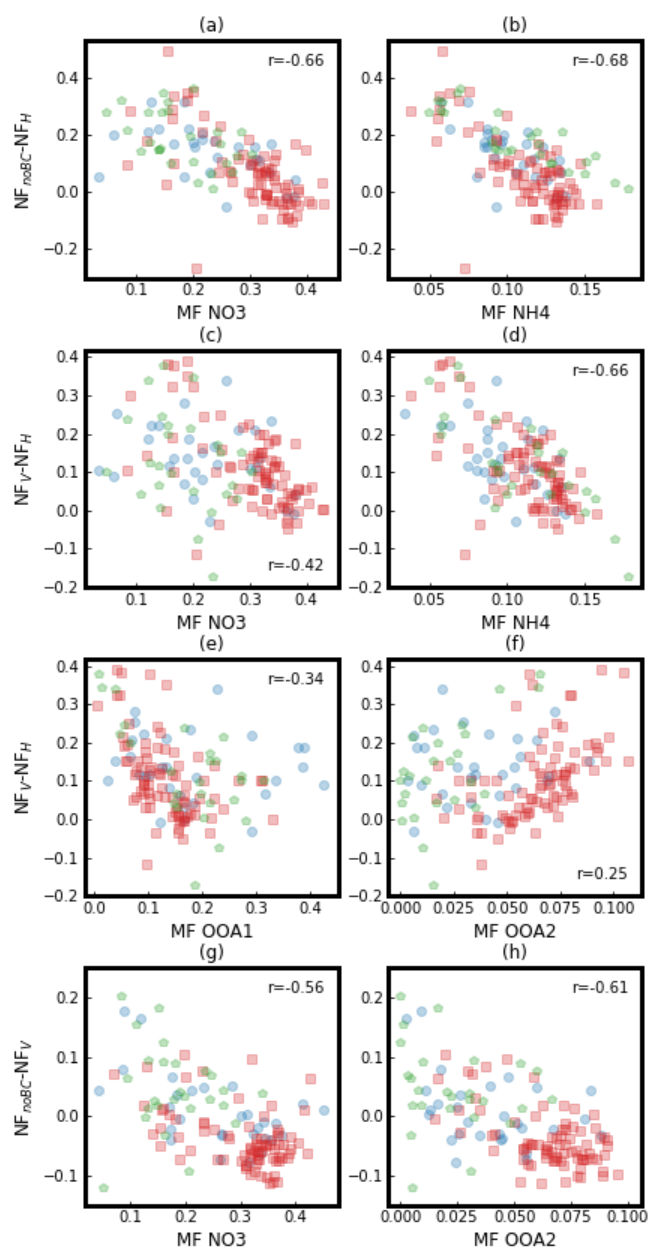
1067

Figure 7. The correlations between the difference among the four aerosol mixing state parameters at particle size 200 nm and mass fractions (MFs) of biomass burning organic aerosol (**BBOA**) and fossil fuel organic aerosols (**FFOA**) during different periods (moderately polluted period: blue circle; heavily polluted period: red square; clean period: green pentagon), with r representing correlation coefficient.

Figure 8. The correlation between the four aerosol mixing state parameters and mass fraction (MF) of secondary aerosol (SA) components during different periods (moderately polluted period: blue dot or circle; heavily polluted period: red x or square; clean period: green plus or pentagon), with r representing correlation coefficient. SA components include secondary organic aerosols (SOA), sulfate (SO_4), nitrate (NO_3), and ammonium (NH_4)

1077

Figure 9. The correlation between the difference among the four aerosol mixing state parameters and mass fraction (MF) of secondary aerosol (SA) chemical components during different periods. OOA1 and OOA2 are two secondary organic aerosol (SOA) factors resolved from aerosol mass spectrometer (AMS) measurements using the Positive Matrix Factorization (PMF) technique. Moderately polluted period: blue circle; heavily polluted period: red square; clean period: green pentagon.
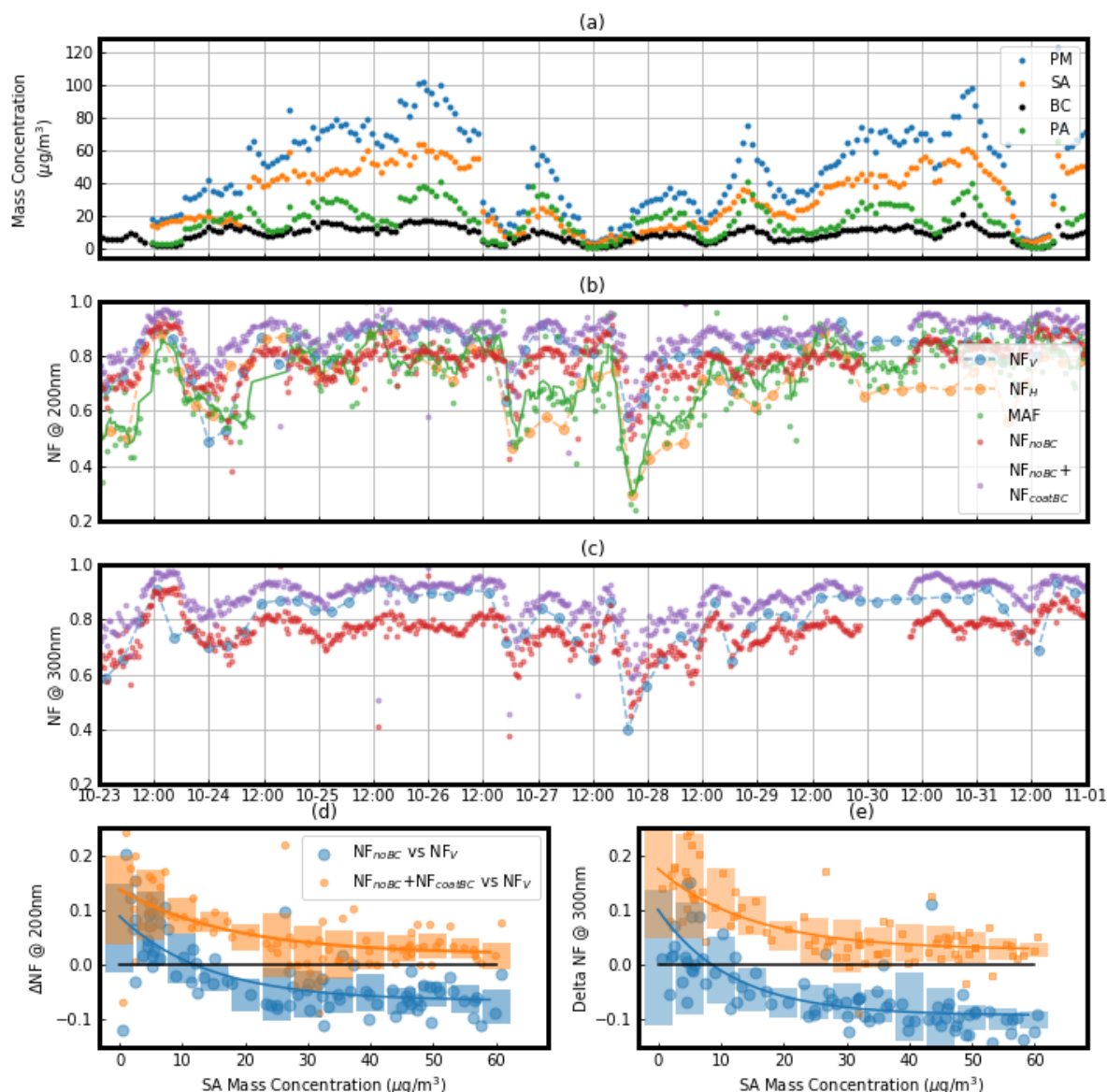
Figure 10. Variations of different aerosol mixing state parameters during the pollution accumulation process. **(a)** The time series of mass concentrations of non-refractory PM$_1$ (NR-PM$_1$), secondary aerosols (SAs) (including inorganic ions and secondary organic aerosols (SOA)), primary organic aerosols (POA) and black carbon (BC) (identified by colors and markers). **(b and c)** The variations of different aerosol mixing state parameters (identified by colors and markers) at particle size 200 nm **(b)** and 300 nm **(c)**. **(d and e)** The variations of the difference between NF$_V$ and NF$_{noBC}$ (NF$_V$-NF$_{noBC}$, blue large circle) and the difference between NF$_V$ and NF$_{noBC}$+NF$_{CBC}$ (NF$_V$-(NF$_{noBC}$+NF$_{CBC}$), yellow small circle) with the mass concentration of SA at particle size 200 nm **(d)** and 300 nm **(e)** **NF$_{CBC}$:** Number Fraction of thickly coated black carbon (BC) particles.